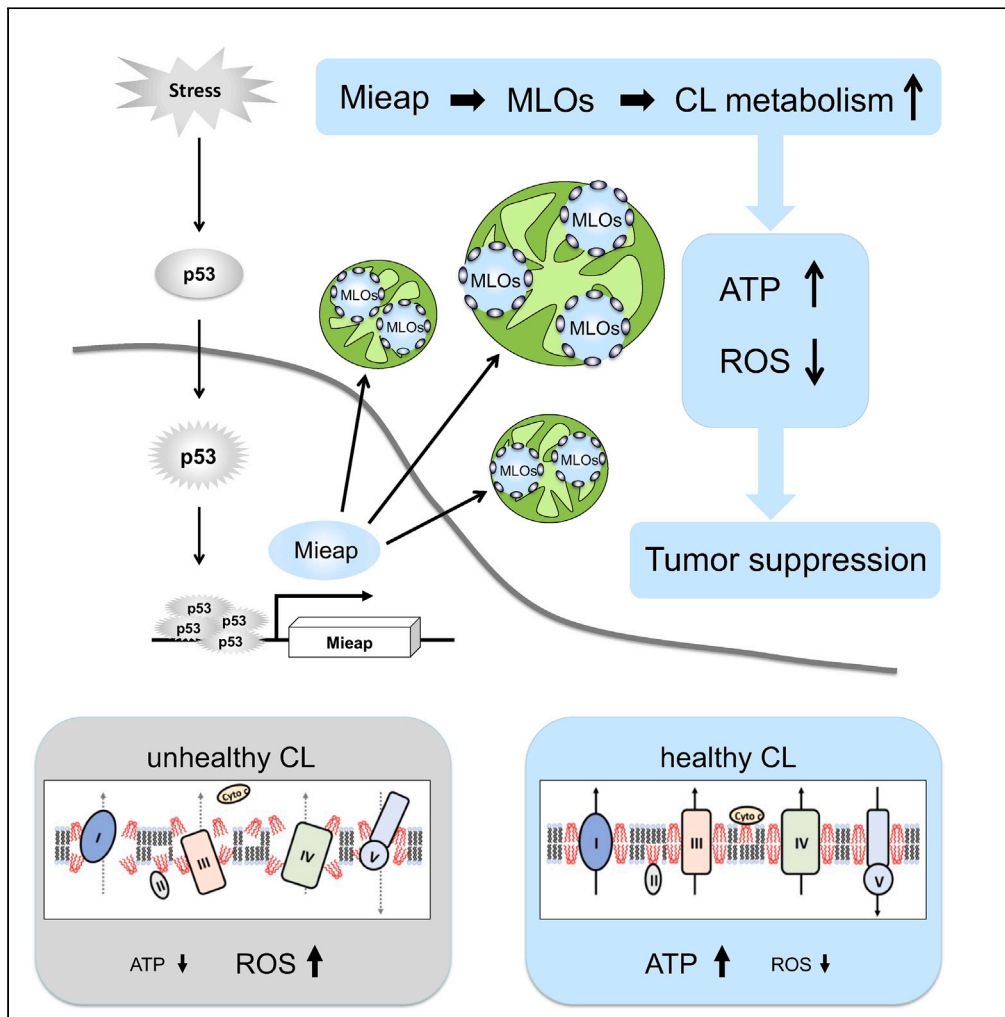**Article**

Mieap forms membrane-less organelles involved in cardiolipin metabolism

Naoki Ikari,
Katsuko Honjo,
Yoko Sagami,
Yasuyuki
Nakamura,
Hirofumi Arakawa

harakawa@ncc.go.jp

Highlights

Mieap maintains mitochondrial quality by regulating cardiolipin metabolism

Mieap BCs compartmentalize and facilitate cardiolipin biosynthesis and remodeling

Mieap BCs consist of two distinct phases containing either enzymes or substrates

Enzymatic reactions occur at interface between enzyme phase and substrate phase

Article

Mieap forms membrane-less organelles involved in cardiolipin metabolism

Naoki Ikari,[1] Katsuko Honjo,[1] Yoko Sagami,[1] Yasuyuki Nakamura,[1] and Hirofumi Arakawa[1,2,*]

SUMMARY

Biomolecular condensates (BCs) are formed by proteins with intrinsically disordered regions (IDRs) via liquid-liquid phase separation. Mieap/Spata18, a p53-inducible protein, participates in suppression of colorectal tumors by promoting mitochondrial quality control. However, the regulatory mechanism involved remains unclear. Here, we report that Mieap is an IDR-containing protein that drives formation of BCs involved in cardiolipin metabolism. Mieap BCs specifically phase separate the mitochondrial phospholipid, cardiolipin. Mieap directly binds to cardiolipin *in vitro*. Lipidomic analysis of cardiolipin suggests that Mieap promotes enzymatic reactions in cardiolipin biosynthesis and remodeling. Accordingly, four cardiolipin biosynthetic enzymes, TAMM41, PGS1, PTPMT1, and CRLS1 and two remodeling enzymes, PLA2G6 and TAZ, are phase-separated by Mieap BCs. Mieap-deficient cells exhibit altered crista structure, leading to decreased respiration activity and ATP production in mitochondria. These results suggest that Mieap may form membrane-less organelles to compartmentalize and facilitate cardiolipin metabolism, thus potentially contributing to mitochondrial quality control.

INTRODUCTION

Biomolecular condensates (BCs) in cells are also known as liquid droplets because of their liquid-like nature. BCs are composed of proteins, nucleic acids, and other macromolecular components,[1–3] and they are formed by proteins with intrinsically disordered regions (IDRs) via liquid-liquid phase separation (LLPS). Importantly, BCs function as membrane-less organelles (MLOs) that compartmentalize and facilitate cellular biological reactions. BCs are not surrounded by lipid bilayers, which enable facile exchange of reactants and products with their surroundings, expediting biological reactions in cells. Furthermore, theoretically, BCs are able to appear and disappear within a cell in response to cellular stress and/or subcellular circumstances, exhibiting spatiotemporally dynamic properties. On the basis of these features, the concept of MLOs is fundamentally different from the long-standing concept of membrane-bound organelles, such as nuclei, lysosomes, mitochondria, and endoplasmic reticulum, which are stable structures that segregate biomolecules and biological reactions using lipid bilayer membranes. Multiple MLOs may exist within a cell, possibly regulating cellular biological reactions and activities, including transcriptional regulation,[4] signal transduction,[5,6] immunity,[7] centrosome activity,[8] and mitosis.[9] This list is rapidly growing.

Metabolic reactions are believed to be highly organized through spatiotemporal clustering and compartmentalization of sequential enzymes and substrates/intermediates at subcellular sites, which maximizes efficiency of linked reactions.[10] Without this mechanism, small, toxic intermediates, derived from metabolic reactions, rapidly diffuse throughout the cytoplasm. Thus, the concept of subcellular compartmentalization of metabolic reactions has been anticipated for a long time. It was initially conceived as a "metabolon," a structural-functional complex of sequential metabolic enzymes and substrates/intermediates.[11] The "metabolon" concept predicted that sequential enzymes and cellular structural elements form a supramolecular complex for metabolic reactions. In fact, many studies have demonstrated that enzyme clustering *in vivo* may facilitate sequential enzymatic metabolic reactions.[12–15] Among them, "purinosomes" involved in purine metabolism, were the first demonstration of enzyme clustering, revealed by live-cell imaging of six sequential enzymes for *de novo* purine synthesis.[16] Although MLOs that compartmentalize and expedite metabolic reactions in cells could address regulatory mechanisms for sequential metabolic reactions, there has been no clear evidence for metabolic MLOs until now.

Cardiolipin (CL) is an important phospholipid for the following reasons. [1] It is a phospholipid dimer, with two phosphate residues and four fatty acyl chains.[17] [2] Because of this unique structure, it forms a cone shape, contributing to curvature of the lipid membrane and to maintenance of mitochondrial cristae.[18] [3] CL is the only phospholipid that is specific to mitochondria and is mainly located at the inner mitochondrial membrane and contact sites.[18] [4] CL interacts with many mitochondrial membrane proteins, including electron transport chain complexes involved in oxidative phosphorylation, and the ADP/ATP carrier. Interaction with CL promotes activity of these proteins.[18] [5] CL stabilizes the structural assembly and activity of respiratory super-complexes at the inner mitochondrial membrane.[19] [6] It interacts with cytochrome *c* at the outer surface of the inner mitochondrial membrane, which supports cellular viability by maintaining stable respiratory

[1]Division of Cancer Biology, National Cancer Center Research Institute, 5-1-1 Tsukiji, Chuo-ku, Tokyo 104-0045, Japan
[2]Lead contact
*Correspondence: harakawa@ncc.go.jp

ATP production and inducing apoptosis, respectively.[19] Therefore, control of CL quality and quantity appears to be important for various mitochondrial functions.

Altered CL metabolism and/or deterioration of CL quality and quantity due to CL metabolic enzyme deficiency causes various mitochondrial dysfunctions in eukaryotes ranging from yeast to mammals.[20,21] Specifically, Barth syndrome is a human disease caused by mutations in the TAZ gene encoding tafazzin, the enzyme responsible for CL remodeling.[22] Clinical symptoms of Barth syndrome patients include cardiomyopathy, skeletal muscle weakness, neutropenia, and growth retardation. Barth syndrome models, including lymphoblasts and induced pluripotent stem cells derived from patients, exhibit abnormal crista structures, decreased respiration activity, and increased reactive oxygen species (ROS) generation in mitochondria.[23,24] This implies that substantial regulation of CL metabolic reactions is required to maintain mitochondrial functions and prevent diseases. However, the regulatory mechanism for CL metabolic reactions is unknown.

Mitochondria-eating protein (Mieap, also denominated SPATA18) was originally identified as a p53-inducible protein. Its mRNA expression is directly regulated by the tumor suppressor, p53, in response to various cellular stresses, including DNA damage.[25] Mieap expression is lost in nearly 50% of human cancer cell lines due to promoter methylation. Mieap-deficient LS174T colorectal cancer cells generate higher levels of mitochondrial ROS and synthesize less ATP. Mitochondrial ROS in Mieap-deficient colorectal cancer and gastric cancer cells enhances migration and invasiveness of cancer cells under hypoxic conditions.[26,27] Mieap deficiency promotes intestinal tumors in Apc[Min/+] mice.[28] Tumors in Mieap-deficient ApcMin/+ mice reveal abnormal mitochondrial morphology, such as large size, round shape, and disordered cristae. Mieap expression is defective in thyroid oncocytic cell tumors, which accumulate abnormal mitochondria in tumor cells.[29] Mieap-regulated mitochondrial quality control is inactivated in tumor tissues of nearly 70% of colorectal cancer and 25% of breast cancer patients.[26,30] These observations suggest that Mieap suppresses tumors via mitochondrial quality control. However, the mechanism underlying regulation of mitochondrial quality control by Mieap remains unclear.

Here, we report that Mieap is an IDR-containing protein that drives BC formation in mitochondria. Mieap BCs phase separates the mitochondrial phospholipid, CL. The present findings suggest that Mieap BCs function as MLOs that compartmentalize and promote CL synthesis and remodeling reactions, leading to stabilization of oxidative phosphorylation and suppression of mitochondrial ROS generation. Thus, we suggest that the Mieap-CL axis is the regulatory mechanism for efficient CL metabolic reactions and/or CL quality and quantity control, forming MLOs that govern mitochondrial quality control by regulating CL synthesis and remodeling. Dysregulation of this pathway leads to mitochondrial dysfunction due to CL alterations, causing a variety of diseases and/or pathologies, including cancer and obesity.

RESULTS

Mieap forms mitochondrial BCs

Mieap has been reported to form vacuole-like structures, designated as Mieap-induced vacuoles (MIVs).[31] To confirm this hypothesis, we performed the IF experiment on structures comprising EGFP-Mieap. EGFP-Mieap reproducibly formed green condensates, while antibodies (anti-Mieap antibody and anti-GFP antibody) produced ring-shaped staining around the green condensates (Figure S1A). Thus, we suspected that antibodies are unable to permeabilize EGFP-Mieap condensates.

We performed additional IF using anti-FLAG antibody for the MIV structures, which comprise N-FLAG-Mieap (N-terminal FLAG-tagged Mieap protein) and C-FLAG-Mieap (C-terminal FLAG-tagged Mieap protein). Ring-shaped staining was observed with N-FLAG-Mieap but not C-FLAG-Mieap (Figure S1B), suggesting that Mieap may be positioned with its N-terminal domain facing outward at the surface of the condensates.

Using transmission electron microscopy (TEM), MIV structures appeared to consist of two phases: a dominant electron-dense phase that stained strongly with OsO_4, and an OsO_4-negative, electron-lucent minor phase (Figure S1C). In immunoelectron microscopy (IEM) analysis with anti-Mieap antibody, gold colloid staining indicated that Mieap protein was distributed over the major electron-dense phase (Figure S1D). Thus, both fluorescent tagging and antigen-antibody reactions confirmed that Mieap forms protein condensates.

Mieap condensates exhibited spherical or oval shapes, fusion, and multi-phase structure consisting of two phases: a Mieap-containing phase and a Mieap-depleted phase (Figures S1A, S1C, S1D, and Video S1). These characteristics, and their propensity to fuse, are not contradictory to a notion that Mieap condensates have liquid-like properties, suggesting that these structures are droplets.[3] Therefore, we designate Mieap-induced structures as Mieap BCs (Mi-BCs).

To clarify the spatial relationship between Mi-BCs and mitochondria, we performed live-cell imaging using cells co-expressing EGFP-Mieap and an outer mitochondrial membrane marker, mApple-TOMM20. mApple-TOMM20 entirely surrounded Mi-BCs, suggesting that Mieap possibly forms condensates in mitochondria (Figure 1 and Video S2).

Mieap is an IDR-containing protein with potential to drive LLPS

We performed *in silico* sequence analyses. Mieap orthologs were found in eukaryotes but not in bacteria, archaea, or viruses (Figure 2A).[32] Hence, the Mieap function evolved in eukaryotes. Moreover, among eukaryotes, Mieap orthologs were found in metazoans but not in fungi (Figure 2A), suggesting that Mieap is beneficial to multicellular organisms.

Using prediction tools,[33–35] we determined that Mieap has four IDRs occurring around two coiled-coil (CC) domains (amino acids 92–311: IDR1 to IDR3) and in the C-terminus (amino acids 499–538: IDR4) (Figures 2B–2E), suggesting that Mieap can potentially drive LLPS.[3]

All four IDRs are enriched in arginine (R, positively charged) and serine (S, uncharged polar) (Figure 2B). Additionally, IDR1 is enriched in aspartic acid (D, negatively charged), and IDR2 is enriched in glutamic acid (E, negatively charged). D and E were mixed with positively
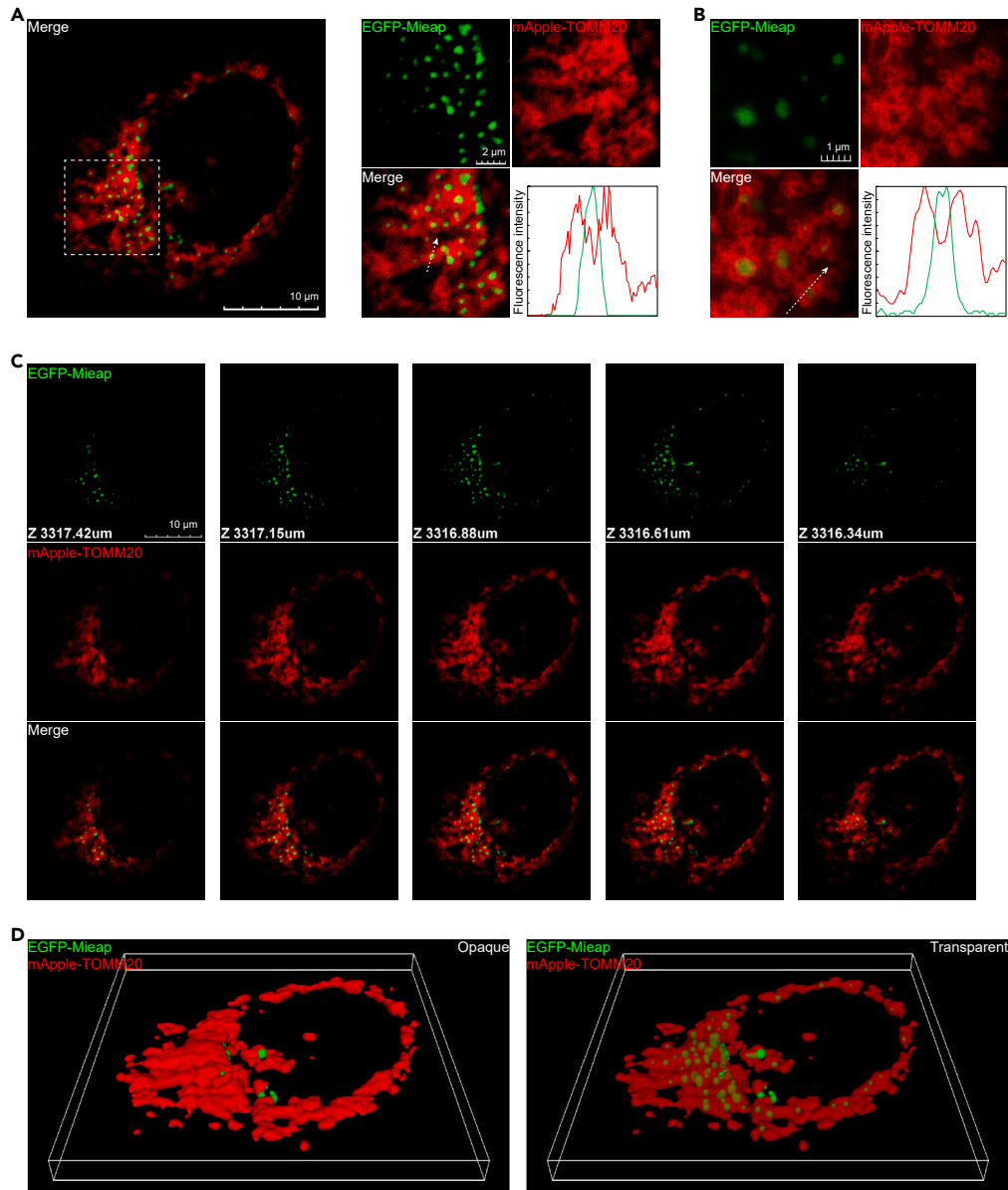
Figure 1. Mieap forms mitochondrial biomolecular condensates

(A) Live-cell imaging and the 3D reconstruction showing the spatial relationship between the Mi-BCs (EGFP-Mieap) and the mitochondrial outer membranes visualized with mApple-TOMM20. The A549 cells were co-infected with Ad-EGFP-Mieap and Ad-mApple-TOMM20. Left: a cell image. Right: higher magnification of the area indicated by the dashed square in the left panel and a line-scan of fluorescence intensities along the dashed arrow. Scale bars, 10 μm (left panel) and 2 μm (right panel). See also Video S2.

(B) Super-resolution images showing the spatial relationship between Mi-BCs (EGFP-Mieap) and mitochondrial outer membranes visualized with mApple-TOMM20. Scale bar, 1 μm.

(C) z stack images of the cell in (A). Scale bar, 10 μm.

(D) 3D reconstruction of the cell shown in (A). See also Video S2.

charged residues in IDR1 and IDR2, respectively. In contrast, IDR3 and IDR4 formed clusters of positively charged residues, characterized by repeats of R and S (Figures 2B–2E).[36]

Although amino acid sequences of the IDRs are evolutionarily divergent compared to the structured regions, the distribution of IDRs and clusters of positively charged residues in IDR3 and IDR4 are evolutionarily conserved (Figures 2C, 2E, and S2).[37] In addition, there is an evolutionarily conserved hydropathic character in the Mieap sequence as a whole, the N-terminal half being hydrophilic and the C-terminal half being hydrophobic (Figures 2D, 2E, and S2).[37] This implies that Mieap protein may act as a cellular biosurfactant.

A
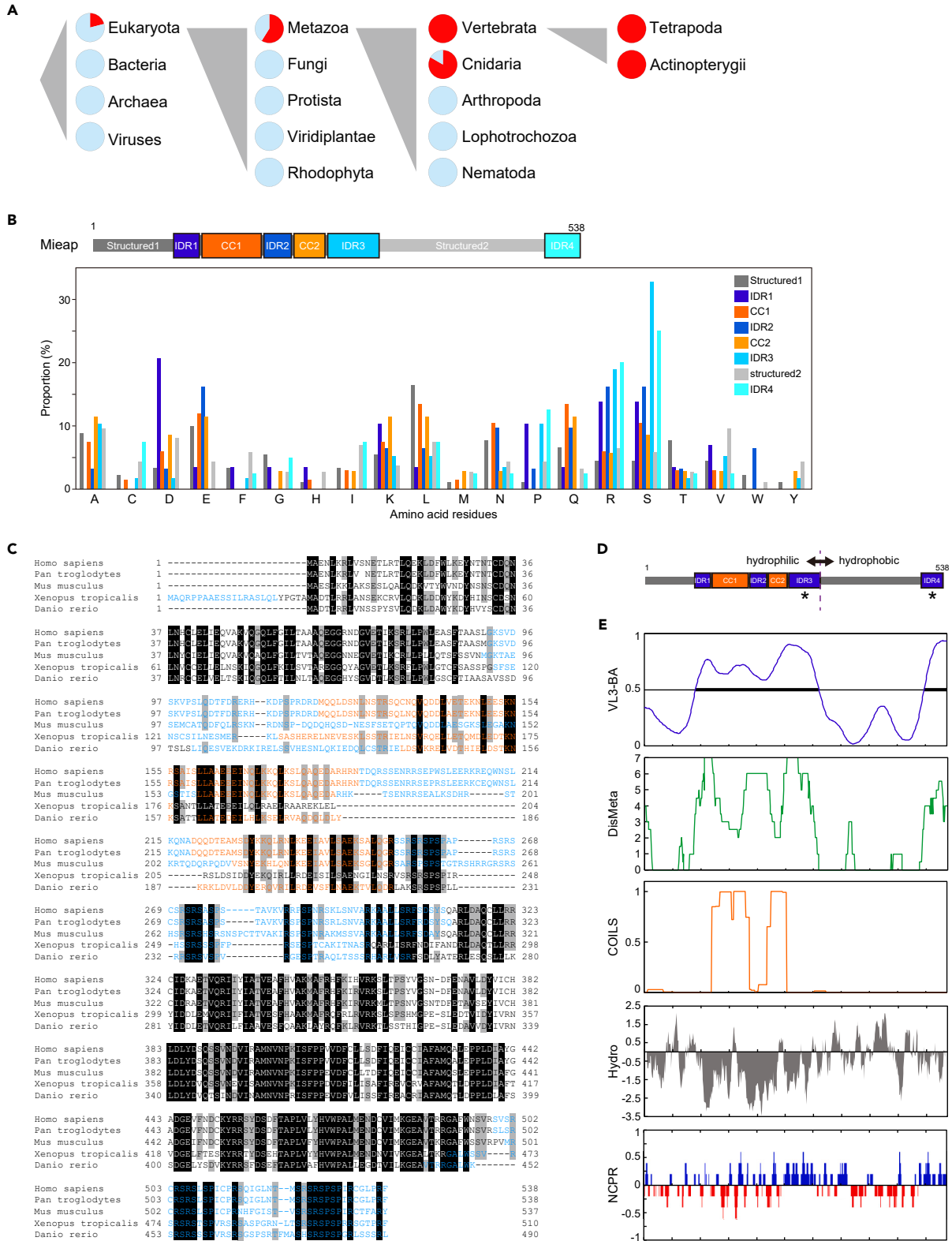

B

C

D

E

Figure 2. Mieap is an IDR-containing protein that has a potential to drive LLPS

(A) Phylogenetic spread of Mieap orthologs annotated with OrthoDB v10. Red sectors indicate present species. Light blue sectors indicate missing species.

(B) Proportion of amino acid residues in each domain of the Mieap protein.

(C) Multiple sequence alignment for Mieap orthologs in representative eukaryotes. Black and gray boxes indicate 100% and 80% identical residues among eukaryotes, respectively. Blue letters indicate IDRs annotated by VL3-BA. Orange letters indicate coiled-coil regions annotated by COILS.

(D) Schematic of the domain structure of Mieap. The dashed vertical line indicates the boundary of gross hydrophilic and hydrophobic halves, separated by IDR3 and the adjacent structured region. Asterisks indicate clusters of positively charged residues.

(E) Sequence analyses of Mieap protein. VL3-BA prediction of IDRs on the amino acid sequence of Mieap, in which bold lines indicate IDRs; DisMeta, meta-prediction of IDRs on the amino acid sequence of Mieap; COILS; coiled-coil regions annotated on the amino acid sequence of Mieap using a 21-residue sliding window; Hydro, hydrophobicity of Mieap using a 9-residue sliding window; NCPR, the linear net charge per residue of Mieap using a 5-residue sliding window.

These molecular features in Mieap IDRs are consistent with the concept of the "evolutionary signature" that Zarin et al. previously proposed.[38] They found that although the amino acid sequences of IDRs are poorly conserved in alignment, most disordered regions contain multiple molecular features that are preserved as an "evolutionary signature", which can be used to predict IDRs from their amino acid sequences in yeast.

Material state and dynamics of Mi-BCs are determined by specific regions of Mieap

To map sites responsible for the physical state and dynamics of Mi-BCs, using a confocal microscope, we examined cells expressing EGFP-Mieap WT (WT) and three deletion-mutant forms, EGFP-Mieap ΔCC, Δ275, and Δ496 (ΔCC, Δ275, and Δ496) (Figure 3A).

To investigate protein dynamics in Mi-BCs, we performed fluorescence recovery after photobleaching (FRAP) studies for WT, ΔCC, Δ275, and Δ496 condensates. During observations up to 60 s after spot-bleaching, with the bleaching depth being 82.2 ± 8.1%, fluorescence intensity of WT, ΔCC, Δ275, and Δ496 condensates recovered to 9.9 ± 4.0%, 4.0 ± 1.0%, 94.3 ± 4.0%, and 17.8 ± 3.1% of their initial values, respectively (Figures 3B and S3A). Fluorescence recovery of the Δ275 condensates almost achieved their initial value within the 60-s observation period, indicating the most fluid state.

When we performed less intense laser exposure, which reduced the bleaching depth to 21.2 ± 4.4%, fluorescence recovery increased 60 s after spot-bleaching (WT, 50.4 ± 8.8%; ΔCC, 32.6 ± 8.8%; Δ275, 94.9 ± 13.7%; Δ496, 61.5 ± 10.1%) (Figure S3B). The fluorescence recovery rate increased when the number of bleached molecules was small, suggesting that availability may be a rate-limiting factor.

We further examined slow fluorescence recovery up to 15 min. WT and Δ496 condensates showed continuous fluorescence recovery, which reached 80.4 ± 10.2% and 94.0 ± 9.5% of the initial value within 15 min, respectively (Figure 3C). In contrast, ΔCC condensates reached equilibrium at 37.4 ± 6.3% of their initial value within 15 min (Figure 3C). These data suggested that WT condensates, as well as Δ496 condensates, consist mainly of mobile materials, but protein availability from their surroundings is limited. Therefore, FRAP analysis data also suggested that Mi-BCs possibly exist in mitochondria.

Mi-BCs phase-separate the mitochondrial phospholipid, CL

To identify molecules targeted for phase separation by Mi-BCs, we screened available fluorescence-tagged mitochondrial proteins and mitochondrial fluorescence probes using confocal live-cell imaging. EGFP-BNIP3, EGFP-NIX, AcGFP1-Mito, DsRed2-Mito, and SYBR Green I (a probe for mitochondrial DNA) were localized at mitochondria, but none of them were incorporated into to Mi-BCs (Figures 3D–3F and Video S3).

However, 10-N-nonyl acridine orange (NAO) was specifically incorporated into Mi-BCs (Figure 3G and Video S4). NAO targets CL.[39] CL binds to >60 mitochondrial proteins via its hydrophobic and electrostatic interactions.[40] As described previously, positively charged residues are enriched in Mieap IDRs and Mieap has its C-terminal half hydrophobic region. CL carries two negative charge phosphate residues and four hydrophobic fatty acyl chains.[41] Sequence data reveal the amphiphilicity of Mieap, and Mi-BCs consist of an electron-dense phase that is positive for OsO4,[42] according to TEM analysis, suggesting that Mi-BCs may contain unsaturated lipids. Therefore, we suspected that CL is a bona-fide target for phase separation by Mi-BCs.

To determine whether Mieap binds directly to CL, we performed a fat blot assay,[43] in which binding of GST-Mieap to CL, phosphatidylcholine (PC), and phosphatidylethanolamine (PE) was evaluated on lipid-dotted membranes. GST-Mieap bound to CL but not to PC or PE (Figure 3H).

Mi-BCs are possible membrane-less organelles involved in CL metabolism

We performed mass spectrometric analyses of CL in A549 cells with and without enforced expression of exogenous Mieap protein by Ad-Mieap infection. The total amount of CL per cell was higher in Ad-Mieap infected cells than in cells without the infection (Figure 4A). Broad CL species showed higher absolute values in cells infected with Ad-Mieap than in non-infected cells (Figure 4B), suggesting the role of Mieap in CL biosynthesis. In contrast, relative amounts of most CL species did not change. However, Mieap significantly increased the proportions of CL72:5, CL72:6, CL70:6, CL68:5, and CL68:6, and decreased the proportions of CL66:3, CL66:4, CL68:2, CL68:3, CL68:4, and CL70:4 (Figure 4B), suggesting the role of Mieap in CL remodeling. Therefore, these results suggest that Mieap is involved in CL metabolism. Therefore, we speculated that Mi-BCs may function as MLOs to compartmentalize and facilitate CL metabolic reactions. To validate this hypothesis, we examined whether Mi-BCs phase-separate enzymes are sequentially involved in CL metabolism (Figure 4C).[20,44,45]
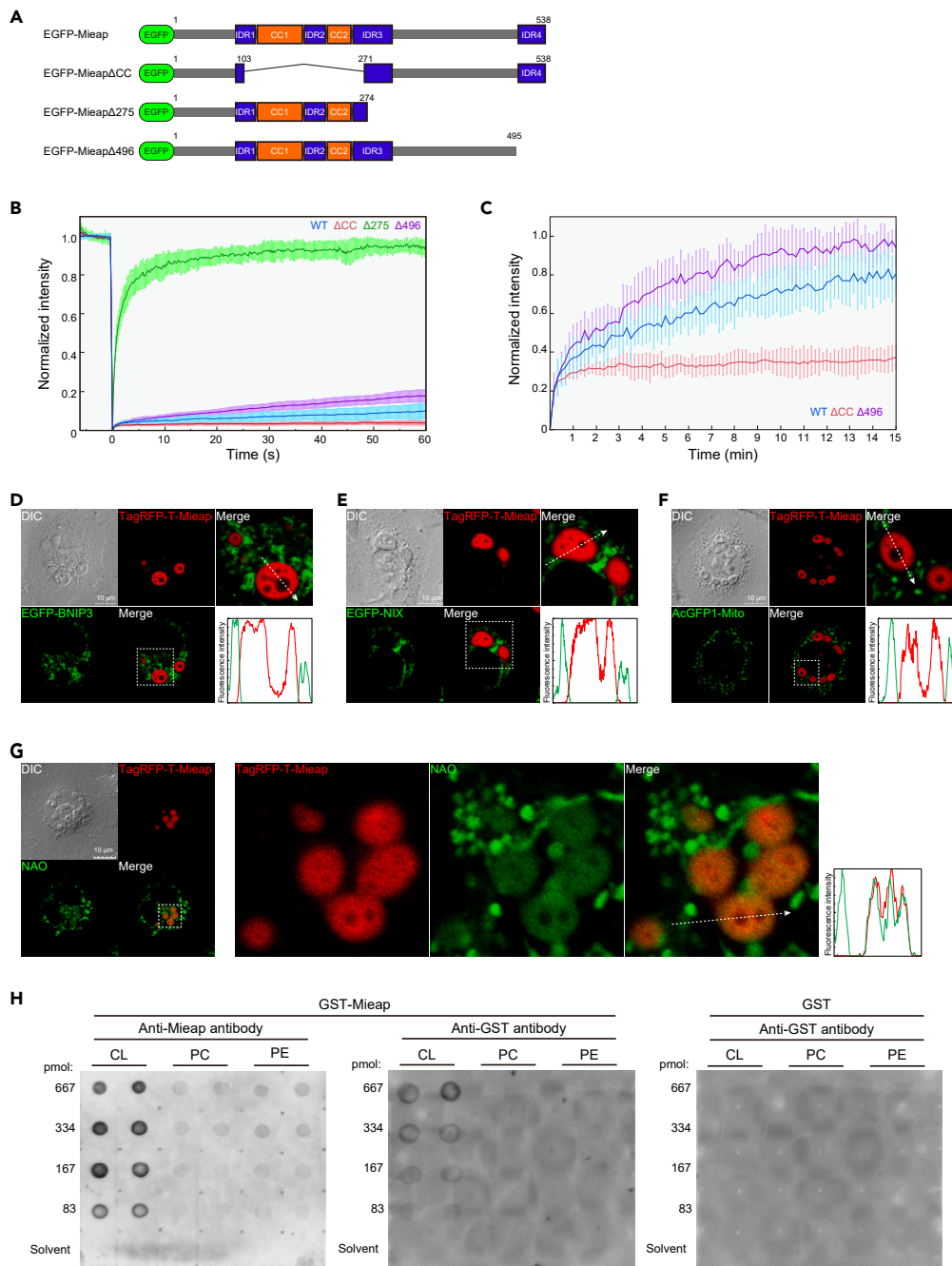
Figure 3. Material state and dynamics of Mi-BCs and phase-separation of the mitochondrial phospholipid cardiolipin by Mi-BCs

(A) EGFP-Mieap and the three deletion-mutant forms. The schematic indicates wild-type (WT) and three deletion mutants (ΔCC, Δ275, and Δ496) of EGFP-Mieap protein. Numbers indicate amino acid residues.

(B) Normalized average fluorescence recovery in the FRAP experiment. EGFP-Mieap, EGFP-Mieap ΔCC, EGFP-Mieap Δ275, and EGFP-Mieap Δ496 were expressed in A549 cells to generate condensates by infection with Ad-EGFP-Mieap, Ad-EGFP-Mieap ΔCC, Ad-EGFP-Mieap Δ275, and Ad-EGFP-Mieap Δ496, respectively. Each condensate was subjected to spot-bleaching using a 488-nm laser at 10% laser power with 11.6 μs/μm exposure time and followed up for 60 s n = 15 condensates for each construct. Data shown are means ± SD.

(C) Normalized average fluorescence recovery in the FRAP experiment with weaker laser exposure as in (B). Laser power was weakened to 1.4% and exposure time was shortened to 1.4 μs/μm. Observation duration was expanded to 15 min after photobleaching entire condensates. n = 10 condensates for each construct. Data shown are means ± SD.

(D–F) Screening of the mitochondrial molecules involved in phase-separation by Mi-BCs. Ad-EGFP-BNIP3 (D), Ad-EGFP-NIX (E), and Ad-AcGFP1-Mito (F) were co-infected with Ad-Mieap and Ad-TagRFP-T-Mieap in A549 cells. Whether each mitochondrial fluorescence probe is phase-separated by Mi-BCs was examined

Thus, we examined involvement of the following EGFP-tagged enzymes required for CL metabolism in Mi-BCs by performing confocal live-cell imaging: EGFP-TAMM41, EGFP-PGS1, EGFP-PTPMT1, and EGFP-CRLS1 (involved in CL biosynthesis); EGFP-PLA2G6 (related to CL hydrolysis by phospholipase A$_2$ activity); and EGFP-TAZ (involved in CL remodeling).[20,45] All of these enzymes localized at mitochondria and were subsequently incorporated into Mi-BCs (Figures 4D–4I and S4A–S4F, and Video S5). Interestingly, all of these CL metabolic enzymes tended to be concentrated in the Mieap-depleted phase in Mi-BCs (Figures 4D–4I and Video S5).

We further examined three additional mitochondrial proteins, PRELI (EGFP-PRELI), mitochondrial protease LONP1 (EGFP-LONP1), and mitochondrial CL hydrolase/mitochondrial phospholipase (MitoPLD)/phospholipase D6 (EGFP-PLD6) (Figures S4G–S4I). PRELI is a mitochondrial carrier of PA for CL production.[44] LONP1 is an AAA mitochondrial protease.[46] PLD6 hydrolyzes CL to generate PA at the outer mitochondrial membrane.[47] EGFP-PRELI was incorporated into Mi-BCs (Figure 4J and Video S5), suggesting that Mi-BCs can also be supplied with PA as a substrate for CL synthesis. Both EGFP-LONP1 and EGFP-PLD6 were located at mitochondria, but neither was incorporated into Mi-BCs (Figures 4K, 4L, and Video S5).

It is important to classify droplet-driver and droplet-client proteins in Mi-BCs. Recently, a bioinformatics-based analysis program (the FuzDrop method) was developed by Fuxreiter's group,[48] which can predict and identify droplet-driver or droplet-client proteins of MLOs. Utilizing this program, we examined if Mieap and all the cardiolipin metabolism-related proteins found in the Mi-BCs (PRELI, TAMM41, PGS1, PTPMT1, CRLS1, PLA2G6, and TAZ) act as drivers or clients. As a result, the program predicted that Mieap acts as a driver of the MLOs and that PRELI, PGS1, CRLS1, PLA2G6, and TAZ act as clients of the MLOs (Figure S5).

Mieap protein is highly concentrated in mitochondrial BCs via its C-terminal hydrophobic region

Since CL biosynthetic enzymes and NAO are located at the inner mitochondrial membrane, we assumed that 3D imaging analysis of the relationship between Mi-BCs and enzymes/NAO would provide the most definitive information on the location of Mi-BCs at mitochondria.

Using fluorescence-tagged CL biosynthetic enzymes, we tried to confirm whether the enlarged Mi-BCs are truly localized within mitochondria by performing live-cell imaging analysis with tomographic 3D reconstruction. As shown in Figure 5A, Videos S6, and S8, enlarged Mi-BCs are fully enveloped by EGFP-TAMM41, signals of which are continuously localized from tubular mitochondria to all around the surfaces of spherical Mi-BCs. Supporting the results of CL biosynthetic enzymes, we further confirmed that NAO is also continuously localized from tubular mitochondria, all round and inside of spherical Mi-BCs (Figure 5B, Videos S7, and S8).

Since CL biosynthetic enzymes tend to localize at the surface of Mi-BCs (Figures 4D–4J), we compared signals of mApple-TOMM20 (the outer mitochondrial membrane) and EGFP-CRLS1 (the inner mitochondrial membrane) around Mi-BCs. As shown in Figures S6A–S6D, the signals of EGFP-CRLS1 were always detected inside the signals of mApple-TOMM20, compared to those of PLD6 (the outer mitochondrial membrane) that are completely consistent with the signals of mApple-TOMM20, suggesting that Mi-BCs are present within mitochondria, possibly facing the inner mitochondrial membrane at their surfaces. Similar results were obtained from the same analysis using another probe for EGFP-TAMM41 (Figure S6E).

Similarly, using EGFP-TAMM41 and NAO as mitochondrial probes, we determined whether ΔCC, Δ275, and Δ496 BCs are located inside mitochondria. As shown in Figures 5C, 5E, Videos S6, and S8, both ΔCC and Δ496 BCs are also fully enveloped by EGFP-TAMM41, whose signals are continuously derived from tubular mitochondria. Moreover, ΔCC and Δ496 BCs are also stained by NAO as a clear picture of tubular mitochondria and each condensate (Figures 5F, 5H, Videos S7, and S8). On the other hand, Δ275 condensates are never related to the signals of EGFP-TAMM41 or NAO (Figures 5D, 5G, and Videos S6–S8). These results suggest that ΔCC and Δ496 BCs are located inside mitochondria, whereas Δ275 BCs are present outside mitochondria.

We further examined partitioning behaviors of WT, ΔCC, Δ275, and Δ496 proteins by performing analysis of Intensity Ratios (IRs) of each protein in BCs and cytoplasm.[49] As shown in Figure 5I, IR values (condensates/cytoplasm) of WT, ΔCC, and Δ496 are 158.62 ± 40.74, 178.81 ± 34.07, 8.29 ± 1.92, and 153.14 ± 25.66 (mean ± SD), respectively. This implies that IR of WT, ΔCC, and Δ496 are more than 18 times higher than that of Δ275. All WT, ΔCC, and Δ496 BCs are localized within mitochondria, whereas Δ275 condensates are present in cytoplasm. Therefore, these IR results suggest that Mieap protein tends to be highly partitioned and concentrated in mitochondrial BCs, and that this propensity is possibly determined by the C-terminal hydrophobic region of Mieap, which could mediate interaction of Mieap with CL/CL-related phospholipids.

Both N-terminal hydrophilic and C-terminal hydrophobic regions are required to generate multi-phase structure of Mi-BCs

To explore the mechanism responsible for multi-phase structure in Mi-BCs, using EGFP-TAMM41, we examined whether CL metabolic enzymes are phase-separated by ΔCC, Δ275, and Δ496 condensates (Figures 6A–6D). As expected, Δ275 condensates did not phase-separate
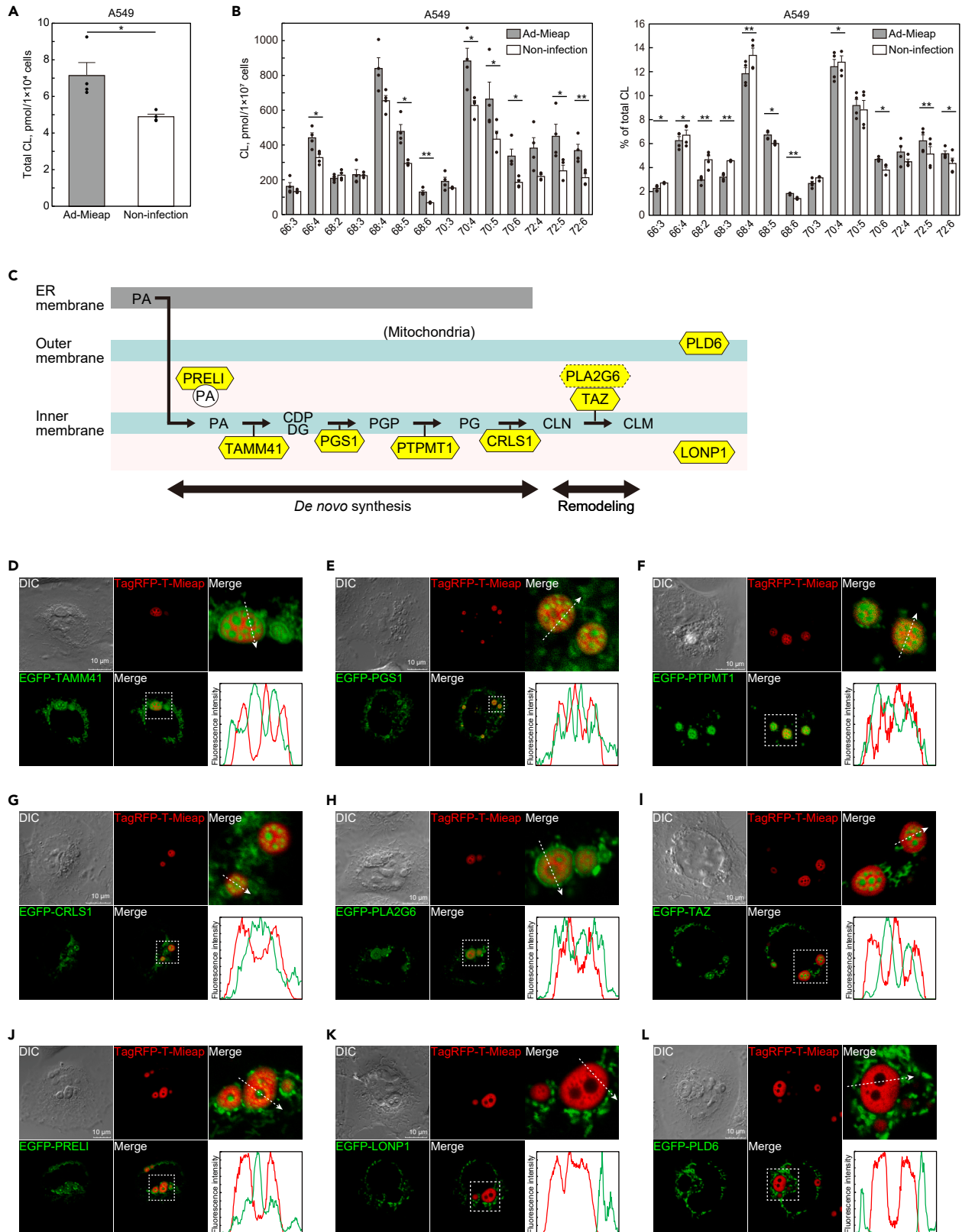
Figure 4. Mi-BCs are possible membrane-less organelles involved in CL metabolism

(A) Quantitative assessment of total CL by mass spectrometric analysis. Uninfected A549 cells or cells infected with Ad-Mieap were subjected to mass spectrometric analysis for CL. Data shown are means $\pm$ SE (n = 4). *p < 0.05, two tailed paired t test.

(B) Quantitative and rate assessments of CL species by mass spectrometric analysis. A549 cells were analyzed as described in (A). Absolute values of selected CL species are shown as amounts of substance per cell (left panel). Relative values of selected CL species are shown as % of total CL (right panel). Data shown are means $\pm$ SE (n = 4). *p < 0.05, **p < 0.01, two tailed paired t test.

(C) The conventional CL metabolic pathway. PA, phosphatidic acid; CDP-DG: cytidine diphosphate diacylglycerol; PGP, phosphatidylglycerophosphate; PG, phosphatidylglycerol; CL_N, nascent cardiolipin; CL_M, mature cardiolipin.

(D–L) Live-cell imaging showing specific phase-separation of CL metabolic enzymes by Mi-BCs. A549 cells were transfected with pEGFP-TAMM41 (D), EGFP-PGS1 (E), EGFP-PTPMT1 (F), EGFP-CRLS1 (G), EGFP-PLA2G6 (H), EGFP-TAZ (I), EGFP-PRELI (J), EGFP-LONP1 (K) and EGFP-PLD6 (L), and subsequently infected with Ad-Mieap and Ad-TagRFP-T-Mieap. EGFP-TAMM41 (D), EGFP-PGS1 (E), EGFP-PTPMT1 (F), EGFP-CRLS1 (G), EGFP-PLA2G6 (H), EGFP-TAZ (I), and EGFP-PRELI (J) were incorporated into the Mieap-depleted phase of Mi-BCs. In contrast, EGFP-LONP1 (K) and EGFP-PLD6 (L) were not incorporated into either the Mieap-containing phase or the Mieap-depleted phase of Mi-BCs. Lower right: line-scan of fluorescence intensities along the dashed arrow. See also Video S5.

EGFP-TAMM41 (Figure 6C). Importantly, although both ΔCC and Δ496 are located in mitochondria, EGFP-TAMM41 was phase-separated and incorporated in the Mieap-depleted phase of Δ496 condensates (Figure 6D), whereas EGFP-TAMM41 was mainly localized across the surfaces of ΔCC condensates, which did not generate multi-phase structures (Figure 6B). These results suggest that both the N-terminal hydrophilic and C-terminal hydrophobic regions are required to form multi-phase droplets. The region of IDR1-3 and two CCs may be critical to the interaction with CL metabolic enzymes to generate the internal enzyme-containing phase (the Mieap-deficient phase) in Mi-BCs.

We further explored the internal structure of the Mieap-depleted phase with EFGP-PGS1 or EGFP-TAMM41. Importantly, we found that CL biosynthetic enzymes, EGFP-PGS1 or EGFP-TAMM41, formed condensates in the Mieap-depleted phase, which wetted the interface between the Mieap-containing phase and the Mieap-depleted phase in either WT or Δ496 BCs (Figures 6E–6L). These results suggest that enzymatic reactions between CL metabolic enzymes and their substrates may occur at the interface between the Mieap-containing phase (Mieap and substrates) and the Mieap-depleted phase (CL metabolic enzymes).

Mieap functions in mitochondrial quality control via regulation of CL metabolism

CL alterations cause mitochondrial dysfunction.[20,21] Mieap is thought to be involved in mitochondrial quality control.[25,26,28,31] Therefore, we hypothesized that Mieap contributes to mitochondrial quality control by regulating CL metabolism. To test this hypothesis, we evaluated mitochondrial status relative to CL integrity in the presence or absence of Mieap protein in cells and mice.

First, we examined respiration rate, mitochondrial ATP production rate, crista morphology, and ROS levels, in control and Mieap-knock-down (KD) LS174T cells under physiological conditions, all of which reflect CL integrity. Flux analysis indicated that respiration and ATP production rates of Mieap-KD cells were significantly lower than those of control cells (Figures 7A, 7B, and S7). TEM analysis revealed that cristae of Mieap-KD cells decreased, and their morphology became indistinct and irregular, compared to that of control cells (Figures 7C and 7D). ROS levels increased in Mieap-KD cells (Figure S8). Consistently, the total amount of CL in control cells was higher than in Mieap-KD cells (Figure 7E), and control cells showed higher absolute values for almost all CL species than Mieap-KD cells (Figure 7F), suggesting the role of Mieap in CL biosynthesis. However, physiological Mieap significantly increased the relative values of CL72:4, CL72:5, CL70:4, CL68:3, and CL68:4, and decreased relative values of CL64:4, CL66:4, CL66:5, CL68:6, and CL70:6 in LS174T cells (Figure 7F), suggesting the role of Mieap in CL remodeling.

Second, utilizing a Mieap-deficient colorectal cancer cell line HCT116, in which the promoter of the Mieap gene is completely methylated,[25] we examined whether re-expression of Mieap affects respiration rate and mitochondrial ATP production rate in these cells. As shown in Figures 7G–7J and S7, re-expression of Mieap protein by Ad-Mieap infection significantly increased respiration rate and mitochondrial ATP production in HCT116 cells.

Third, we analyzed crista morphology in kidney and liver tissues of Mieap-knockout (KO) mice by performing TEM analysis. In Mieap$^{-/-}$ kidney mitochondria, irregularly dilated lamellar structures without distinct OsO_4 staining were observed (Figures 7K and 7M). A decrease in normal crista structure was a common characteristic of Mieap$^{-/-}$ mitochondria in the kidney and liver (Figures 7K–7N).

Fourth, we performed a large-scale cross-sectional observation of 1,225 Mieap$^{+/+}$, Mieap$^{+/-}$, and Mieap$^{-/-}$ mice to identify long-term consequences of Mieap deficiency. Average body weights of Mieap$^{+/-}$ and Mieap$^{-/-}$ mice were higher than those of Mieap$^{+/+}$ mice throughout their lives (Figures 8A and S9). Differences were prominent during middle and old age, from 44 to 104 weeks (Figure 8B) (mean value $\pm$ SE; Mieap$^{+/+}$ 33.065 $\pm$ 0.425 g [n = 149], Mieap$^{+/-}$ 34.048 $\pm$ 0.302 g [n = 295], Mieap$^{-/-}$ 35.090 $\pm$ 0.392 g [n = 175]), but particularly during middle age, from 53 to 62 weeks (Figure 8C) (mean value $\pm$ SE; Mieap$^{+/+}$ 31.048 $\pm$ 0.759 g [n = 49], Mieap$^{+/-}$ 33.378 $\pm$ 0.496 g [n = 115], Mieap$^{-/-}$ 34.579 $\pm$ 0.645 g [n = 68]). Although the differences of mean values among three groups are statistically significant, they are very small. In addition, as seen in Figure S9, body weights of individual Mieap-deficient mice are very variable. Consistent with these features, we could not find any differences of food uptake and locomotor activities between wild-type and Mieap-deficient mice.

To evaluate gender bias in these mice, we further examined whether there is any difference in obesity between male and female in Mieap-deficient mice. As shown in Figures S10A, S10B, S10E, S10F, Mieap-deficient mice of both sexes developed obesity that persisted throughout their lives. This obesity was prominent during middle and old age, from 44 to 104 weeks (Figures S10E and S10G) (mean value $\pm$ SE; Mieap$^{+/+}$ 36.060 $\pm$ 0.509 g [n = 74], Mieap$^{+/-}$ 36.835 $\pm$ 0.371 g [n = 139], Mieap$^{-/-}$ 37.679 $\pm$ 0.461 g [n = 90] in male, and Mieap$^{+/+}$ 30.110 $\pm$ 0.514 g
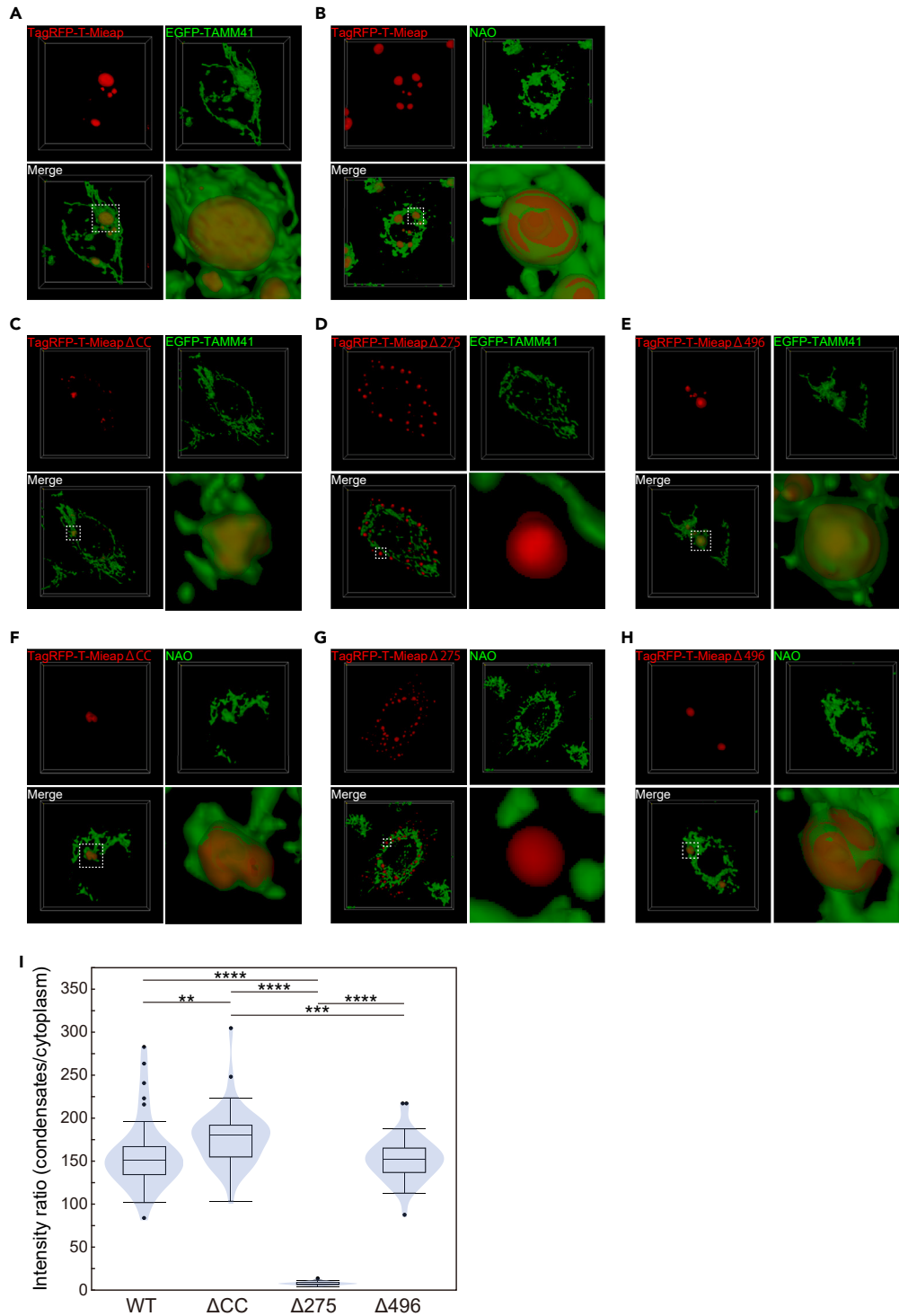
Figure 5. Mieap protein is highly concentrated in mitochondrial BCs via its C-terminal hydrophobic region

(A and B) 3D reconstruction showing the spatial relationship between Mi-BCs and mitochondrial inner membrane visualized with EGFP-TAMM41 (A) or NAO (B). See also Videos S6, S7, and S8.

(C–H) 3D reconstruction showing the spatial relationship between BCs formed by ΔCC, Δ275, or Δ496, and mitochondrial inner membrane visualized with EGFP-TAMM41 (C–E) or NAO (F–H). See also Videos S6, S7, and S8. HeLa cells were transfected with pEGFP-TAMM41 to visualize mitochondrial inner membrane, and subsequently infected with Ad-TagRFP-T-Mieap WT (A), Ad-TagRFP-T-Mieap ΔCC (C), Ad-TagRFP-T-Mieap Δ275 (D), or Ad-TagRFP-T-Mieap Δ496 (E) to form BCs.

Figure 5. Continued

A549 cells were infected with Ad-TagRFP-T-Mieap WT (B), Ad-TagRFP-T-Mieap ΔCC (F), Ad-TagRFP-T-Mieap Δ275 (G), or Ad-TagRFP-T-Mieap Δ496 (H) to form BCs, and after BCs were formed, mitochondrial inner membrane was visualized by NAO.

(I) Partitioning behavior of EGFP-Mieap WT, ΔCC, Δ275, or Δ496 protein in condensates and cytoplasm, displayed in violin plot. A549 cells were infected with Ad-EGFP-Mieap WT, ΔCC, Δ275, or Δ496 to generate condensates, and after BCs were formed, the intensity ratio (IR) of condensates and cytoplasm was measured. n = 40 cells for each construct in A549 cells. **p < 0.01, ***p < 0.001, ****p < 0.0001, two tailed Student's *t* test. When the data were visualized using violin plots, boxplots were overlaid. The center line in the box indicates the median. The bottom and top of the box indicate the 25th and 75th percentiles. The whiskers extend 1.5 times the interquartile range (IQR) from the top and bottom of the box unless the minimum and maximum values are within the IQR. The values which fall above or below the whiskers are plotted individually as outliers.

[n = 75], Mieap$^{+/-}$ 31.565 ± 0.356 g [n = 156], Mieap$^{-/-}$ 32.350 ± 0.483 g [n = 85] in female), but more remarkably during middle age, from 53 to 62 weeks (Figures S10D and S10H), (mean value ±SE; Mieap$^{+/+}$ 34.365 ± 0.952 g [n = 23], Mieap$^{+/-}$ 36.714 ± 0.633 g [n = 52], Mieap$^{-/-}$ 37.238 ± 0.731 g [n = 39] in male, and Mieap$^{+/+}$ 28.113 ± 0.813 g [n = 26], Mieap$^{+/-}$ 30.625 ± 0.522 g [n = 63], Mieap$^{-/-}$ 31.002 ± 0.770 g [n = 29] in female). These results suggest that the obesity trend in Mieap-deficient mice occurs regardless of sex.

To confirm that the body weight gain in Mieap-deficient mice reflects increased fat deposition, we evaluated the amount of subcutaneous fat and intra-abdominal fat (perigonadal fat and perirenal fat) in four representative litter pairs (Mieap$^{+/+}$ and Mieap$^{-/-}$). As shown in Figure S11, the amount of fat in Mieap$^{-/-}$ mice is obviously higher than in Mieap$^{+/+}$ mice in all four pairs. Therefore, we suggest that the body weight gain in Mieap-deficient mice is due to obesity.

Reduced mitochondrial respiratory activity in adipose tissues has been suggested as a factor contributing to obesity.[50] Brown fat tissue (BAT) is essential to heat production via both its respiratory activity, which generates a proton gradient, and uncoupling protein 1 (UCP1)-mediated proton leakage across the mitochondrial inner membrane.[51,52] Therefore, BAT mitigates obesity. Importantly, as a CL-binding protein, activity of UCP1 is stabilized by CL.[53] Thus, we examined the status of mitochondrial cristae in BAT of Mieap$^{-/-}$ mice. We confirmed that normal crista structure was significantly decreased in Mieap-deficient BAT (Figures 8D and 8E).

These results of Figures 8A–8E, S10, and S11, taken together, suggest that obesity may be a long-term consequence of mitochondrial dysfunction due to CL alteration in tissues of Mieap-deficient mice, including BAT (Figure 8F).

Finally, we examined endogenous Mieap expression *in vivo*. To achieve this, utilizing WT, Mieap-KO, and p53-KO mice and anti-mouse Mieap antibody, we performed immunohistochemical (IHC) analysis on 20 tissues/organs, including brain (cerebellar cortex), brain (cerebro-ventricle), heart, liver, kidney, lung, stomach, small intestine, pituitary gland, eye, harderian gland, salivary gland, thyroid, bladder, testis, epididymis, seminal vesicle, prostate, uterus, and fallopian tube. Specific signals of Mieap were detected in all examined tissues/organs by comparing data from WT and Mieap-KO (Figures S12–S16). Interestingly, basal expression of endogenous Mieap protein is not regulated by p53. Importantly, patterns of Mieap expression are remarkably similar to those of cytochrome *c* in IHC and IF (Figures S12–S16), suggesting that endogenous Mieap protein is localized at mitochondria.

Considering the results of partitioning behavior of Mieap and its mutants in Figure 5I, since endogenous Mieap protein is expressed at mitochondria in most tissues/organs, endogenous Mieap protein could be highly concentrated in mitochondrial droplets under physiological conditions. This implies that physiological Mieap protein likely has a significant impact on mitochondrial quality control in all tissues/cells containing mitochondria. On the basis of all these results, we suggest that Mieap maintains mitochondrial quality by regulating CL metabolism.

DISCUSSION

Although the importance of multi-enzyme complexes in metabolic enzyme reactions has been recognized, it remains unclear how this complex of enzymes efficiently and safely enables sequential enzymatic reactions by preventing diffusion of intermediates. A recent report suggested that concentration of multiple enzymes and substrates/intermediates in a restricted space could mediate efficient sequential enzymatic reactions by preventing diffusion of intermediates.[54] In that model, multiple copies of upstream and downstream enzymes involved in sequential enzymatic reactions are assembled into a single cluster, called an "agglomerate." According to this model, "once an upstream enzyme produces an intermediate, although the probability of the intermediate being processed by any individual downstream enzymes is low, the probability that the intermediate will be processed by one of the many downstream enzymes in the "agglomerate" can be high."[54] Therefore, based on this model, molecular crowding of enzymes, substrates, and intermediates in a restricted space could enable efficient sequential enzymatic reactions mediated by multiple enzymes.

The "agglomerate" concept is promising, but an important question remains. How can so many diverse molecules, including multiple enzymes, substrates, and intermediates, be gathered, concentrated, and compartmentalized in a single restricted space? What drives formation of the "agglomerate"? We speculate that BCs could organize agglomerates as metabolic BCs.[55] Accumulating evidence suggests that BCs function as MLOs, which promote biochemical reactions by concentrating and compartmentalizing enzymes and substrates in cells.[56–60] Since BCs are not surrounded by lipid bilayers, theoretically, they exhibit spatiotemporal dynamic properties within a cell in response to cellular stress and/or subcellular circumstances. More importantly, while BCs contain hundreds of molecules, a few scaffold proteins can drive formation of these MLOs.[1] If there are proteins that can organize metabolic BCs as scaffolds,[57] these agglomerates could enable efficient metabolic reactions.

In the present study, we obtained the following evidence supporting our hypothesis that Mi-BCs may regulate CL metabolism: [1] Mieap drives formation of droplets in mitochondria. [2] Mi-BCs phase-separate NAO, a specific probe for CL, and Mieap directly binds to CL. [3] Mi-BCs compartmentalize and concentrate all four sequential enzymes for CL biosynthesis (TAMM41, PGS1, PTPMT1, and CRLS1). [4] Mi-BCs

Figure 6. Both N- and C-terminal regions of Mieap are required to generate the multi-phase structure of Mi-BCs

(A–D) Comparison of phase-separating behaviors on the CL metabolic enzyme, TAMM41 (EGFP-TAMM41), between BCs formed by TagRFP-T-Mieap WT (A), ΔCC (B), Δ275 (C), and Δ496 (D). Right: line-scan of fluorescence intensities along the dashed arrow. Scale bars, 10 μm.

(E–H) CL metabolic enzymes wet the interface in the Mieap-depleted phase of Mi-BCs. Distributions of the CL metabolic enzymes, EGFP-PGS1 (E, F) and EGFP-TAMM41 (G, H), in the Mieap-depleted phase of Mi-BCs are shown. Lower right: line-scan of fluorescence intensities along the dashed arrow. Scale bars, 2 μm.

(I–L) CL metabolic enzymes wet the interface in the Mieap Δ496-depleted phase of Δ496-BCs. Distributions of the CL metabolic enzymes, EGFP-PGS1 (I, J) and EGFP-TAMM41 (K, L), in the Mieap Δ496-depleted phase of BCs formed by the Δ496 mutant are shown. Lower right: line-scan as in (E–H). Scale bars, 2 μm.

HeLa cells were transfected with pEGFP-TAMM41 (A–D, G, H, K, and L) or pEGFP-PGS1 (E, F, I, and J), and subsequently infected with Ad-TagRFP-T-Mieap WT (A, E–H), Ad-TagRFP-T-Mieap ΔCC (B), Ad-TagRFP-T-Mieap Δ275 (C), or Ad-TagRFP-T-Mieap Δ496 (D, I–J). After BCs were formed, the relationship between EGFP-TAMM41 and each mutant BCs was analyzed (A–D), or the Mieap-depleted phase was analyzed on wetting of EGFP-PGS1 (E, F, I, J) or EGFP-TAMM41 (G, H, K, and L).

compartmentalize and concentrate two enzymes for CL remodeling (PLA2G6 and TAZ). [5] The presence or absence of Mieap protein is closely related to an increase or decrease in various species of CL, respectively. [6] Mieap protein specifically increases the proportion of several species of CLs. [7] Mieap deficiency is related to changes in crista structure and CL metabolism in cells, and crista structure *in vivo*. This evidence suggests that Mieap is a scaffold protein that drives formation of metabolic BCs to compartmentalize and concentrate enzymes, substrates, and intermediates that are involved in CL biosynthesis and remodeling, leading to molecular crowding within Mi-BCs that promotes efficient catalysis of CL metabolic reactions (Figure 9).[61] Supporting this model, a recently developed bioinformatics-based program[48] (the FuzDrop method) predicted that Mieap acts as a driver protein of MLOs and that PGS1, CRLS1, PLA2G6, and TAZ act as client proteins of MLOs (Figure S5).

Mi-BCs exhibit properties of multi-phase droplets, in which there are two phases, a Mieap-containing phase and a Mieap-depleted phase. Interestingly, CL and Mieap occur in the Mieap-containing phase, whereas all CL biosynthesis and remodeling enzymes, including TAMM41, PGS1, PTPMT1, CRLS1, PLA2G6, and TAZ, are predominantly segregated into the Mieap-depleted phase. This result suggests that substrates, intermediates, and products for CL metabolism do not reside in the same phase as their catalytic enzymes. Such a relationship between substrates and enzymes in multi-phase droplets is not limited to Mi-BCs but is seen in other droplets. In terms of RNA processing droplets formed by FMRP and CAPRIN1, RNA and phosphorylated FMRP form multi-phase droplets, in which the deadenylation enzyme, CNOT7, and the substrate, polyA-RNA, are segregated into different phases, but this leads to faster deadenylation rates.[62]

Why don't substrates and enzymes occur in the same phase of metabolic BCs? A recent study demonstrated that sequestration of enzymes to a membrane-less compartment that is away from, but adjacent to substrates, can accelerate reactions much faster than when the enzymes are mixed with the substrates in the same compartment.[63] Concentration of enzymes and substrates in a single phase might result in substrate inhibition.[63] Therefore, separation of enzymes from their substrates via LLPS could facilitate enzymatic reactions by mitigating substrate inhibition. In this case, the interface between the enzyme and substrate phases would be the site of the reaction.[63] Consistent with this hypothesis, we observed accumulation of CL biosynthetic enzymes such as PGS1 and TAMM41 at the interface of the Mieap-depleted phase (Figures 6E–6L). Therefore, enzymatic reactions of CL enzymes and CL substrates may occur at the interface between the Mieap-containing phase (Mieap and substrates) and the Mieap-depleted phase (CL metabolic enzymes) (Figure 9).[61]

Feric et al. reported the mechanism for generation of multi-phase structures in droplets.[64] By performing *in vivo* and *in vitro* experiments, the authors demonstrated that layered droplet organization is caused by differences in droplet surface tension, facilitating sequential RNA processing reactions in a variety of RNP bodies. In their experiments, F1B and NPM1 formed multi-phase droplets in which F1B droplets tended to be encapsulated within NPM1 droplets. They found that F1B droplets tended to wet hydrophobic surfaces, whereas NPM1 droplets tended to wet hydrophilic surfaces. Wetting refers to the contact between liquids and surfaces, which depends on surface tension. Therefore, in the aqueous phase, F1B droplets with high surface tension tended to be enveloped by NPM1 droplets with lower surface tension.

Since Mieap may be positioned with its N-terminal domain facing outward at the surfaces of Mi-BCs (Figure S1B), Mi-BCs could exist in a hydrophilic environment. If so, according to the theory of Feric et al., the Mieap-containing phase may be enveloped by the Mieap-depleted phase, because the former is more hydrophobic than the latter. However, the authors also pointed out the presence of a surfactant that modulates surface tension alters or inverts the organization of multi-phase droplets. Since Mieap could serve as a biosurfactant, Mieap may modulate the surface tension of the Mieap-containing phase and the Mieap-depleted phase in a hydrophilic environment. Therefore, the relation between the two phases could be inverted in Mi-BCs.

We hypothesize the following model for sequential CL-metabolic reactions promoted by Mieap (Figure 9).[61] Mieap may stably interact with the substrate (PA) via its C-terminal, hydrophobic, structured region, which exhibits a specific, strong interaction. On the other hand, Mieap weakly and transiently interacts with CL-metabolizing enzymes via its N-terminal hydrophilic region, which exhibits multiple interactions. In this model, once Mieap attracts the substrate with its C-terminal region, Mieap enables sequential CL metabolic reactions by transiently interacting with the enzyme corresponding to the substrate at the interface between the Mieap-containing phase and the Mieap-depleted phase, and then changing enzymes until mature CL is produced. Therefore, interactions of the N-terminal hydrophilic region of Mieap with CL enzymes and the C-terminal hydrophobic region of Mieap with CL/CL-related phospholipids may be critical to drive formation of multi-phase organization of Mi-BCs. In summary, (1) concentration of enzymes and substrates, (2) segregation of enzymes and substrates into distinct sub-compartments of metabolic droplets, (3) interfacial catalysis, and (4) biosurfactant activity of Mieap could foster highly efficient sequential enzymatic reactions for CL metabolism in Mi-BCs. We suggest that Mi-BCs may be the first known metabolic MLOs to regulate CL synthesis and remodeling (Figure 9).[61]
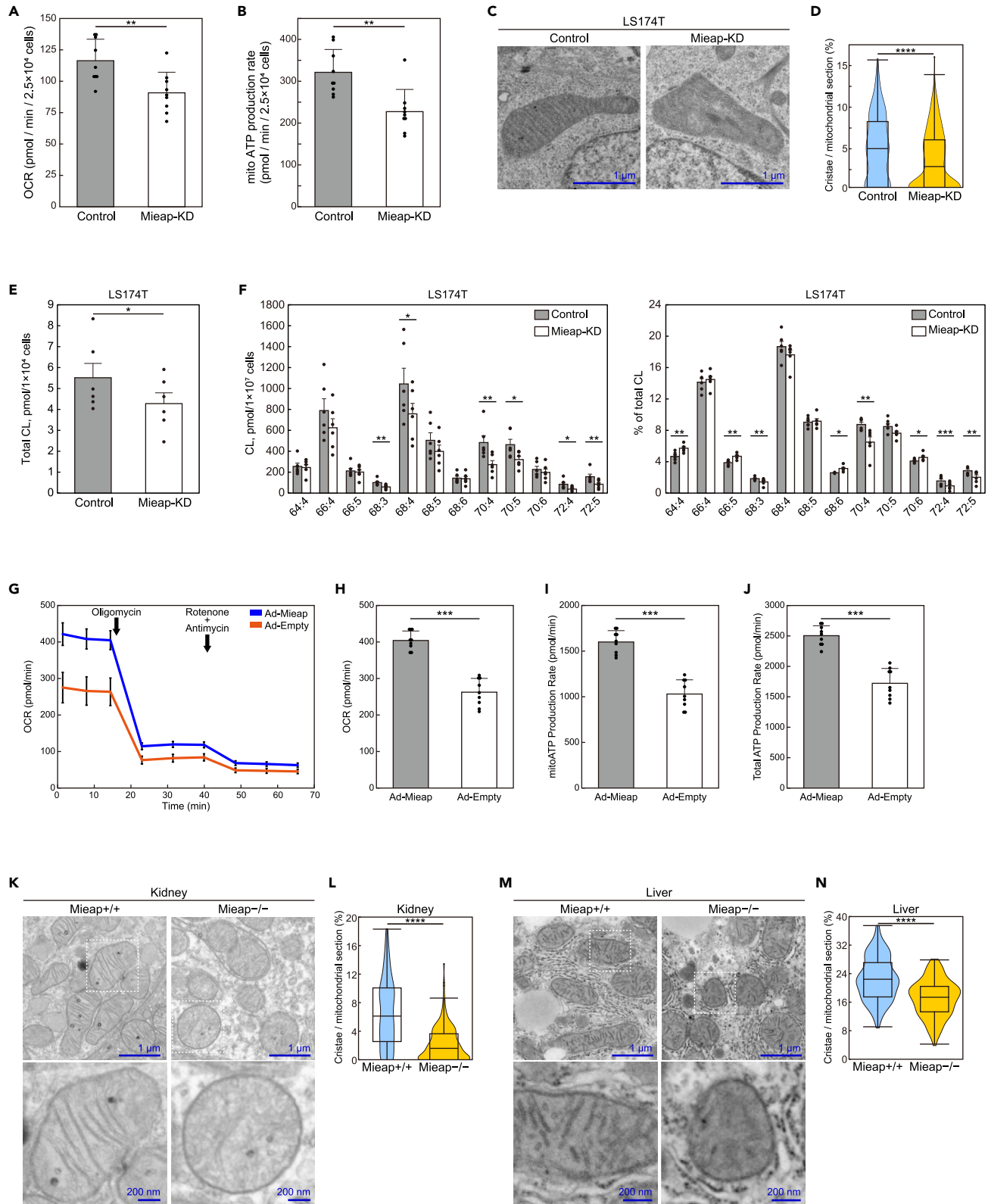
Figure 7. Mieap contributes to mitochondrial quality control by promoting CL metabolism

(A) Oxygen consumption rates (OCR) of LS174T-cont and Mieap-KD cells under normal conditions calculated with a flux analyzer. Data are shown as means $\pm$ SD (n = 9).

(B) Mitochondrial ATP production rates of LS174T-cont and Mieap-KD cells under normal conditions calculated with a flux analyzer, using a Seahorse XF real-time ATP rate assay. Data are shown as means $\pm$ SD (n = 9).

(C) Morphology of mitochondria of LS174T-cont and Mieap-KD cells with transmission electron microscopy (TEM). Scale bars, 2 μm.

(D) Ratio of crista area per mitochondrial section of LS174T-cont and Mieap-KD cells. Quantitative data were obtained from cont mitochondria (n = 197) and Mieap-KD mitochondria (n = 329) in TEM images and displayed in a violin plot.

(E) Quantitative assessment of total CL by mass spectrometric analysis. LS174T cells with (Cont) and without (Mieap-KD) endogenous Mieap expressions were subjected to mass spectrometric analysis. Data shown are means $\pm$ SE (n = 6).

(F) Quantitative and rate assessments of CL species by mass spectrometric analysis. LS174T cells were analyzed as described in (E). Absolute values of selected CL species are shown as the amount of substance per cell (left panel). Relative values of selected CL species are shown as % of total CL (right panel). Data shown are means $\pm$ SE (n = 6).

(G) The kinetic profile of the OCR using the Seahorse XF Real-Time ATP rate assay in HCT116 cells infected with Ad-Mieap or Ad-empty.

(H–J) Quantitative assessment of OCR (H), mitochondrial ATP production rates (I), and total ATP production rates (J) of the HCT116 cells as in (G). Data are shown as means $\pm$ SD (n = 9).

(K) Morphology of kidney mitochondria of Mieap$^{+/+}$ and Mieap$^{-/-}$ mice with TEM. Scale bars, 1 μm (upper panels) and 200 nm (lower panels).

(L) Ratios of crista area per mitochondrial section of Mieap$^{+/+}$ and Mieap$^{-/-}$ mouse kidneys. Quantitative data were obtained from Mieap$^{+/+}$ kidney mitochondria (n = 190) and Mieap$^{-/-}$ kidney mitochondria (n = 234) in TEM images and displayed in a violin plot.

(M) Morphology of liver mitochondria of Mieap$^{+/+}$ and Mieap$^{-/-}$ mice with TEM. Scale bars, 1 μm (upper panels) and 200 nm (lower panels).

(N) Ratios of crista area per mitochondrial section of Mieap$^{+/+}$ and Mieap$^{-/-}$ mouse livers. Quantitative data were obtained from Mieap$^{+/+}$ liver mitochondria (n = 146) and Mieap$^{-/-}$ liver mitochondria (n = 134) in TEM images and displayed in a violin plot. (A, B, D, H-J, L, N) **p < 0.01, ***p < 0.001, ****p < 0.0001, two tailed Student's t test. (E, F) *p < 0.05, **p < 0.01, ***p < 0.001, two tailed paired t test. When the data were visualized using violin plots, boxplots were overlaid. The center line in the box indicates the median. The bottom and top of the box indicate the 25th and 75th percentiles. The whiskers extend 1.5 times the interquartile range (IQR) from the top and bottom of the box unless the minimum and maximum values are within the IQR. The values which fall above or below the whiskers are plotted individually as outliers.

BCs are often thought to accelerate enzymatic reaction rate by merely increasing local concentrations of enzymes and substrates (mass action). However, Peeples and Rosen reported that concentrating enzymes and substrates alone results in decreasing enzymatic reaction rates by substrate inhibition due to high concentrations of substrates.[65] They demonstrated that in addition to mass action, a scaffold-induced decrease in K_M is critical to accelerate enzymatic reactions in BCs.[65] In their synthetic system where the SUMOylation enzyme cascade is recruited into engineered condensates, they showed that having both enzyme and substrate bound simultaneously to proximal sites in a scaffold oligomer, which leads to decreased K_M, is required to enhance the enzymatic reaction. Our Mi-BC model is compatible with their findings; however, further investigation of this hypothesis is required.

In the present study, we demonstrated that Mieap-deficient LS174T cells exhibited altered CL metabolism, decreased respiration activity, increased ROS levels, and manifested abnormal crista structure, all of which are consistent with phenotypes induced by CL alteration. We also found that Mieap-deficient mice exhibit decreased numbers and morphological abnormalities of mitochondrial cristae in kidney and liver tissues. Furthermore, our body weight analysis of Mieap$^{+/+}$, Mieap$^{+/-}$, and Mieap$^{-/-}$ mice clarified increased obesity in Mieap-deficient mice, which is likely attributable to mitochondrial dysfunction in various tissues, including BAT. Therefore, we assume that all these phenotypes in Mieap-deficient cells and mice reflect mitochondrial dysfunctions related to abnormal CL metabolism. So far, autophagy and proteostasis are two major mechanisms in mitochondrial quality control.[66] In addition to these, we suggest that the Mieap-regulated pathway is the third mechanism for mitochondrial quality control, in which Mieap maintains integrity of mitochondria by regulating CL metabolism. It accomplishes this through homeostasis of the inner mitochondrial membrane by regulating CL metabolism, stabilizing oxidative phosphorylation, and suppressing mitochondrial ROS generation (Figure 8F).

Previously, we reported that although Mieap-deficient mice did not suffer from intestinal dysfunction, Mieap-deficient Apc$^{Min/+}$ mice exhibited remarkable intestinal tumor generation and malignant transformation, compared to Mieap-WT Apc$^{Min/+}$ mice.[28] Furthermore, mitochondria in Mieap-deficient tumors revealed abnormal morphology, including fewer cristae and enlarged, spherical mitochondria. These results support the role of Mieap in mitochondrial quality control through control of CL metabolism in response to oncogenic stress. In addition to Apc$^{Min/+}$ mice, we also observed tumor suppressive role of Mieap in a thyroid cancer mouse model.[67] Therefore, Mieap-regulated mitochondrial quality control could be critical in tumor suppression by promoting CL metabolism, which leads to upregulation of respiratory activity and downregulation of mitochondrial ROS generation. Considering the role of Mieap in p53 function, we suggest that Mieap could act as a spatiotemporal and dynamic regulator/modulator of CL metabolism to suppress tumor initiation and progression.[61] Recently, we found that Mieap-deficient sperm in Mieap-KO mice cause *in vitro* infertility due to mitochondrial ROS elevation and impaired sperm motility (unpublished data). Therefore, in addition to cancer and obesity, it is possible that alterations of Mieap-regulated mitochondrial quality control also promote infertility (Figure 8F). Further investigation is required to clarify the precise role of Mieap in the regulation of CL metabolism.

A recent study reported that PGS1, PTPMT1, and CRLS1 form a large mitochondrial CL synthesis complex in human cells, with a molecular mass of 700–800 kDa.[68] This large CL synthesis complex includes multiple CL-binding proteins. These observations are very similar to our results that Mi-BCs contain all CL synthesis enzymes (Figures 4D–4I) and several CL-binding proteins (unpublished data). However, IF experiments on PGS1 or CRLS1 in that study indicated that neither PGS1 nor CRLS1 showed visible Mi-BC-like structures in mitochondria.[68] Our results from live-cell imaging of EGFP-fused CL synthesis enzymes, including PGS1 and CRLS1, also showed that none of the EGFP-tagged
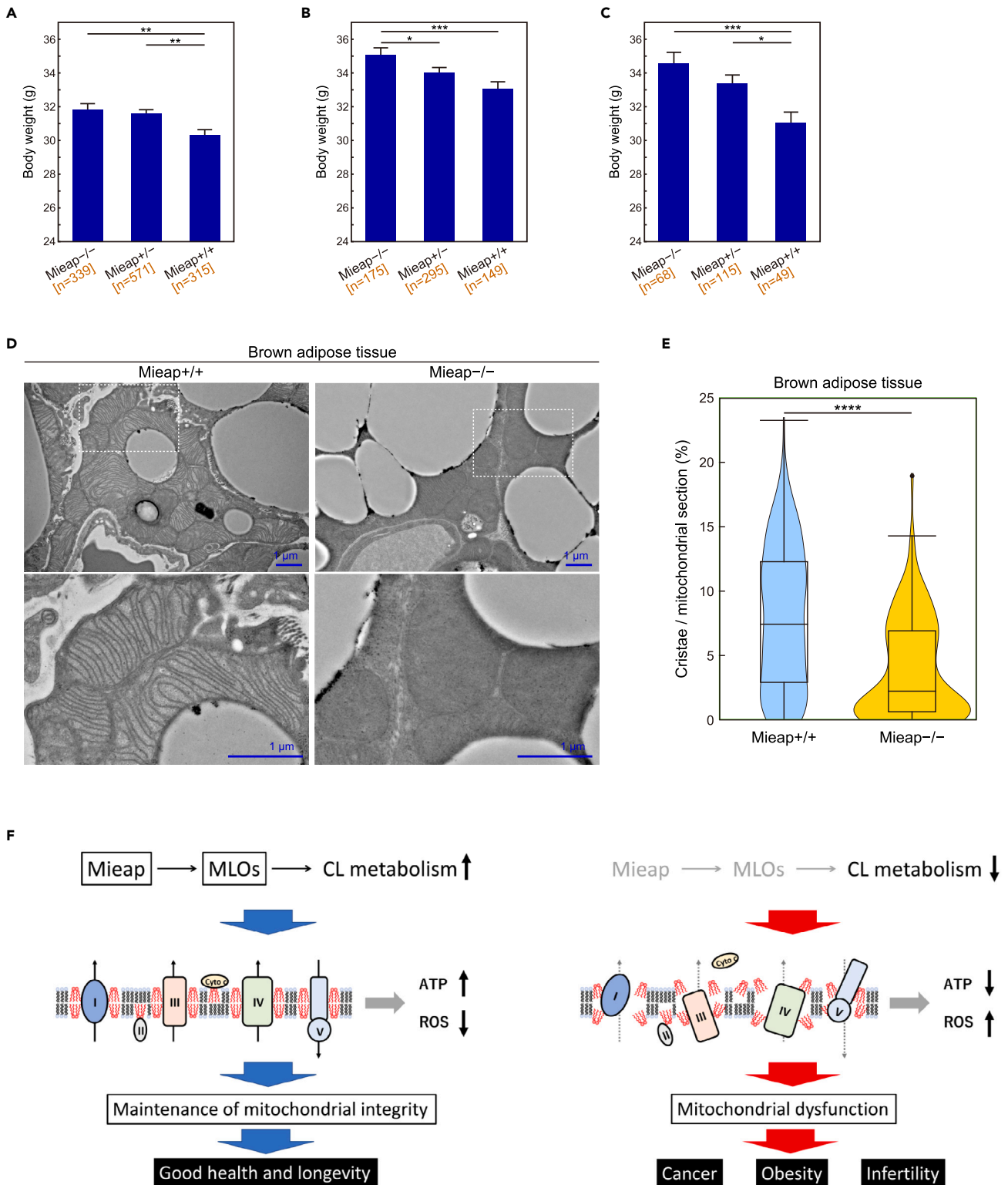
Figure 8. Mieap prevents obesity by maintaining cristae structures of BAT

(A–C) Body weights of Mieap$^{+/+}$, Mieap$^{+/-}$, and Mieap$^{-/-}$ mice (7–130 weeks of age) (A), (44–104 weeks of age) (B), and (53–62 weeks of age) (C). Data shown are means ± SE. *p < 0.05, **p < 0.01, ***p < 0.001, two tailed Student's t test.

(D) Morphology of brown adipose tissue (BAT) mitochondria of Mieap$^{+/+}$ and Mieap$^{-/-}$ mice with TEM. Scale bars, 1 μm.

Figure 8. Continued

(E) The ratio of crista area per mitochondrial section of Mieap$^{+/+}$ and Mieap$^{-/-}$ mice BAT. Quantitative data were obtained from Mieap$^{+/+}$ BAT mitochondria (n = 181) and Mieap$^{-/-}$ BAT mitochondria (n = 129) in TEM images and displayed in a violin plot. ****p < 0.0001, two tailed Student's t test. The center line in the box indicates the median. When the data were visualized using violin plots, boxplots were overlaid. The bottom and top of the box indicate the 25th and 75th percentiles. The whiskers extend 1.5 times the interquartile range (IQR) from the top and bottom of the box unless the minimum and maximum values are within the IQR. The values which fall above or below the whiskers are plotted individually as outliers.

(F) A hypothetical model for mitochondrial quality control via the Mieap-MLOs-CL metabolism axis.

CL synthesis enzymes exhibit visible Mi-BC-like structures. Therefore, we suggest that under physiological conditions, the minute size of Mi-BCs or possibly layered, membrane-less organelles induced by Mieap may compartmentalize and facilitate CL metabolic reactions *in vivo*, efficiently maintaining enzymatic reactions.

Supporting this hypothesis, we confirmed specific expression of Mieap protein *in vivo* in 20 tissues/organs that contain mitochondria (Figures S12–S16). Importantly, patterns of endogenous Mieap expression are very similar to those of cytochrome *c*, suggesting that endogenous Mieap protein is localized at mitochondria. On the other hand, the results of partitioning behaviors of Mieap and its mutants indicated that Mieap protein is highly concentrated in mitochondrial droplets (Figure 5I). These results, taken together, imply that the physiological Mieap protein may be condensed into micro-Mi-BCs that are distributed all through mitochondria to promote CL metabolism. Therefore, we suggest that physiological Mieap protein may have a significant impact on mitochondrial quality control in all tissues/cells containing mitochondria. Further investigation is needed to clarify the full picture of physiological membrane-less organelles involved in CL metabolism.

Limitations of the study

In the current study, we have demonstrated a possible model of MLOs involved in CL biosynthesis and remodeling in over-expression experiments with various fluorescence-tagged proteins. However, we have not yet showed a real picture of physiological Mi-BCs *in vivo*. Utilizing newly developed technologies for imaging, physiological Mi-BCs must be explored and demonstrated in future study. For this purpose, it is important to establish mNeonGreen-Mieap knock-in mice to analyze endogenous Mieap protein. Furthermore, it is also critical to show that artificial Mi-BCs really contain CL metabolic enzymes and substrates/intermediates and that CL enzymatic reactions are promoted in Mi-BCs in the next study. Matrix granules within mitochondria might be potential physiological MLOs involved in CL metabolism, which have been suggested to be stores of material (mainly phospholipids such as CL) of inner mitochondrial membrane from a long time ago.[69,70] Therefore, further examination on the role of mitochondrial matrix granules in CL metabolism is very important.

STAR★METHODS

Detailed methods are provided in the online version of this paper and include the following:

- KEY RESOURCES TABLE
- RESOURCE AVAILABILITY
  - Lead contact
  - Materials availability
  - Data and code availability
- EXPERIMENTAL MODEL AND STUDY PARTICIPANT DETAILS
  - Cell lines
  - Animals
- METHOD DETAILS
  - Plasmid construction
  - Transfection
  - Recombinant adenovirus construction
  - Adenoviral infection
  - Immunocytochemistry
  - Histological analysis
  - Transmission electron microscopy (TEM)
  - Post-embedding immunoelectron microscopy
  - Amino acid sequence analyses of Mieap protein
  - Analyses of confocal microscopy image data
  - FRAP experiments
  - Calculation of intensity ratio
  - Expression and purification of GST and GST-Mieap
  - Lipid-binding analysis
  - Lipid preparation
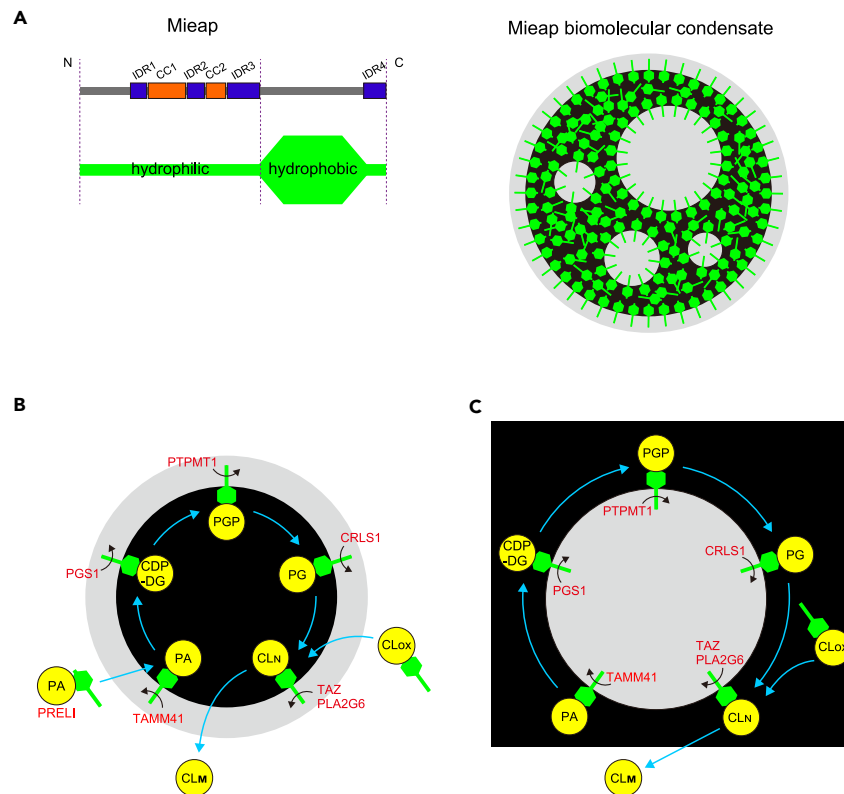 - Mass spectrometric analyses of CL
  - Real-time ATP rate assay

Figure 9. Hypothetical models for Mieap-mediated sequential enzymatic reactions in CL metabolism

(A) Hypothetical model of biosurfactant activity of Mieap. Mieap (green) exists in the Mieap-containing phase (lipid phase) (black), as a "scaffold" protein and/or as a potential "biosurfactant." At the boundary between the surfaces of Mi-BCs (aqueous phase) and the Mieap-containing phase (lipid phase) or between the Mieap-containing phase (lipid phase) and the Mieap-depleted phase (aqueous phase), the hydrophilic N-terminal end of Mieap always faces the aqueous phase at the boundary.

(B and C) Hypothetical model for Mieap-mediated sequential enzymatic reactions in CL metabolism. Black areas indicate the Mieap-containing phase (lipid phase) containing CL and Mieap. Gray areas indicate the Mieap-depleted (aqueous phase) containing enzymes. Sequential reactions occur at the interface between the surface of Mi-BCs (aqueous phase) and the Mieap-containing phase (lipid phase) (B) or between the Mieap-containing phase (lipid phase) and the Mieap-containing phase (aqueous phase) (C). Once Mieap (green) stably interacts with PA via its C-terminal region, one of the enzymes transiently and weakly interacts with the N-terminal region of Mieap. When Mieap interacts with TAMM41, PA is converted to CDP-DG. Such reactions between biosynthetic enzymes and corresponding substrates could be repeated until mature CL is produced. Concentration of enzymes and substrates at Mi-BC surfaces, segregation of enzymes and substrates into distinct sub-compartments of Mi-BCs, interfacial catalysis, and biosurfactant activity of Mieap may enable efficient sequential reactions for CL metabolism. PA, phosphatidic acid; CDP-DG: cytidine diphosphate diacylglycerol; PGP, phosphatidylglycerophosphate; PG, phosphatidylglycerol; CLOX, oxidized cardiolipin; CLN, nascent cardiolipin; CLM, mature cardiolipin.

- ○ Flow cytometric analysis
- ○ Primers
- ● QUANTIFICATION AND STATISTICAL ANALYSIS
- ○ FRAP data quantification
- ○ Crista data quantification
- ○ Statistical analysis
- ○ Data visualization

SUPPLEMENTAL INFORMATION

Supplemental information can be found online at https://doi.org/10.1016/j.isci.2024.108916.

ACKNOWLEDGMENTS

AUTHOR CONTRIBUTIONS

N.I. and H.A. conceptualization; N.I., K.H., Y.S., Y.N., and H.A. data curation; H.A. funding acquisition; N.I., K.H., Y.S., Y.N., and H.A. formal analysis; N.I. and H.A. investigation; H.A. project administration; H.A. supervision; N.I. and H.A. writing – original draft.

DECLARATION OF INTERESTS

The authors declare no competing interests.

REFERENCES

1. Shin, Y., and Brangwynne, C.P. (2017). Liquid phase condensation in cell physiology and disease. Science 357, eaaf4382.
2. Boeynaems, S., Alberti, S., Fawzi, N.L., Mittag, T., Polymenidou, M., Rousseau, F., Schymkowitz, J., Shorter, J., Wolozin, B., Van Den Bosch, L., et al. (2018). Protein Phase Separation: A New Phase in Cell Biology. Trends Cell Biol. 28, 420–435.
3. Alberti, S., Gladfelter, A., and Mittag, T. (2019). Considerations and Challenges in Studying Liquid-Liquid Phase Separation and Biomolecular Condensates. Cell 176, 419–434.
4. Sabari, B.R., Dall'Agnese, A., Boija, A., Klein, I.A., Coffey, E.L., Shrinivas, K., Abraham, B.J., Hannett, N.M., Zamudio, A.V., Manteiga, J.C., et al. (2018). Coactivator condensation at super-enhancers links phase separation and gene control. Science 361, eaar3958.
5. Case, L.B., Zhang, X., Ditlev, J.A., and Rosen, M.K. (2019). Stoichiometry controls activity of phase-separated clusters of actin signaling proteins. Science 363, 1093–1097.
6. Huang, W.Y.C., Alvarez, S., Kondo, Y., Lee, Y.K., Chung, J.K., Lam, H.Y.M., Biswas, K.H., Kuriyan, J., and Groves, J.T. (2019). A molecular assembly phase transition and kinetic proofreading modulate Ras activation by SOS. Science 363, 1098–1103.
7. Du, M., and Chen, Z.J. (2018). DNA-induced liquid phase condensation of cGAS activates innate immune signaling. Science 361, 704–709.
8. Woodruff, J.B., Ferreira Gomes, B., Widlund, P.O., Mahamid, J., Honigmann, A., and Hyman, A.A. (2017). The centrosome is a selective condensate that nucleates microtubules by concentrating tubulin. Cell 169, 1066–1077.e10.
9. Rai, A.K., Chen, J.X., Selbach, M., and Pelkmans, L. (2018). Kinase-controlled phase transition of membraneless organelles in mitosis. Nature 559, 211–216.
10. Welch, G.R. (1977). On the role of organized multienzyme systems in cellular metabolism: a general synthesis. In Prog. Biophys. Mol. Biol. (Elsevier), pp. 103–191.
11. Srere, P.A. (1987). Complexes of sequential metabolic enzymes. Annu. Rev. Biochem. 56, 89–124.
12. Jin, M., Fuller, G.G., Han, T., Yao, Y., Alessi, A.F., Freeberg, M.A., Roach, N.P., Moresco, J.J., Karnovsky, A., Baba, M., et al. (2017). Glycolytic Enzymes Coalesce in G Bodies under Hypoxic Stress. Cell Rep. 20, 895–908.
13. Lee, H., DeLoache, W.C., and Dueber, J.E. (2012). Spatial organization of enzymes for metabolic engineering. Metab. Eng. 14, 242–251.
14. Kohnhorst, C.L., Kyoung, M., Jeon, M., Schmitt, D.L., Kennedy, E.L., Ramirez, J., Bracey, S.M., Luu, B.T., Russell, S.J., and An, S. (2017). Identification of a multienzyme complex for glucose metabolism in living cells. J. Biol. Chem. 292, 9191–9203.
15. Schmitt, D.L., and An, S. (2017). Spatial Organization of Metabolic Enzyme Complexes in Cells. Biochemistry 56, 3184–3196.
16. An, S., Kumar, R., Sheets, E.D., and Benkovic, S.J. (2008). Reversible compartmentalization of de novo purine biosynthetic complexes in living cells. Science 320, 103–106.
17. Macfarlane, M.G. (1958). Structure of cardiolipin. Nature 182, 946.
18. Ikon, N., and Ryan, R.O. (2017). Cardiolipin and mitochondrial cristae organization. Biochim. Biophys. Acta Biomembr. 1859, 1156–1163.
19. Paradies, G., Paradies, V., De Benedictis, V., Ruggiero, F.M., and Petrosillo, G. (2014). Functional role of cardiolipin in mitochondrial bioenergetics. Biochim. Biophys. Acta 1837, 408–417.
20. Ren, M., Phoon, C.K.L., and Schlame, M. (2014). Metabolism and function of mitochondrial cardiolipin. Prog. Lipid Res. 55, 1–16.
21. Paradies, G., Paradies, V., Ruggiero, F.M., and Petrosillo, G. (2019). Role of cardiolipin in mitochondrial function and dynamics in health and disease: Molecular and pharmacological aspects. Cells 8, 728.
22. Saric, A., Andreau, K., Armand, A.S., Møller, I.M., and Petit, P.X. (2015). Barth syndrome: from mitochondrial dysfunctions associated with aberrant production of reactive oxygen species to pluripotent stem cell studies. Front. Genet. 6, 359.
23. Acehan, D., Xu, Y., Stokes, D.L., and Schlame, M. (2007). Comparison of lymphoblast mitochondria from normal subjects and patients with Barth syndrome using electron microscopic tomography. Lab. Invest. 87, 40–48.
24. Dudek, J., Cheng, I.F., Balleininger, M., Vaz, F.M., Streckfuss-Bömeke, K., Hübscher, D., Vukotic, M., Wanders, R.J.A., Rehling, P., and Guan, K. (2013). Cardiolipin deficiency affects respiratory chain function and organization in an induced pluripotent stem cell model of Barth syndrome. Stem Cell Res. 11, 806–819.
25. Miyamoto, Y., Kitamura, N., Nakamura, Y., Futamura, M., Miyamoto, T., Yoshida, M., Ono, M., Ichinose, S., and Arakawa, H. (2011). Possible Existence of Lysosome-Like Organella within Mitochondria and Its Role in Mitochondrial Quality Control. PLoS One 6, e16054.
26. Kamino, H., Nakamura, Y., Tsuneki, M., Sano, H., Miyamoto, Y., Kitamura, N., Futamura, M., Kanai, Y., Taniguchi, H., Shida, D., et al. (2016). Mieap-regulated mitochondrial quality control is frequently inactivated in human colorectal cancer. Oncogenesis 4, e181.
27. Okuyama, K., Kitajima, Y., Egawa, N., Kitagawa, H., Ito, K., Aishima, S., Yanagihara, K., Tanaka, T., and Noshiro, H. (2019). Mieap-induced accumulation of lysosomes within mitochondria (MALM) regulates gastric cancer cell invasion under hypoxia by suppressing reactive oxygen species accumulation. Sci. Rep. 9, 2822.
28. Tsuneki, M., Nakamura, Y., Kinjo, T., Nakanishi, R., and Arakawa, H. (2015). Mieap suppresses murine intestinal tumor via its mitochondrial quality control. Sci. Rep. 5, 12472.
29. Mussazhanova, Z., Shimamura, M., Kurashige, T., Ito, M., Nakashima, M., and Nagayama, Y. (2020). Causative role for defective expression of mitochondria-eating protein in accumulation of mitochondria in thyroid oncocytic cell tumors. Cancer Sci. 111, 2814–2823.
30. Gaowa, S., Futamura, M., Tsuneki, M., Kamino, H., Tajima, J.Y., Mori, R., Arakawa, H., and Yoshida, K. (2018). Possible role of p53/Mieap-regulated mitochondrial quality control as a tumor suppressor in human breast cancer. Cancer Sci. 109, 3910–3920.
31. Kitamura, N., Nakamura, Y., Miyamoto, Y., Miyamoto, T., Kabu, K., Yoshida, M., Futamura, M., Ichinose, S., and Arakawa, H. (2011). Mieap, a p53-Inducible Protein, Controls Mitochondrial Quality by Repairing or Eliminating Unhealthy Mitochondria. PLoS One 6, e16060.
32. Kriventseva, E.V., Kuznetsov, D., Tegenfeldt, F., Manni, M., Dias, R., Simão, F.A., and Zdobnov, E.M. (2019). OrthoDB v10: sampling the diversity of animal, plant, fungal, protist, bacterial and viral genomes for evolutionary and functional annotations of orthologs. Nucleic Acids Res. 47, D807–D811.
33. Huang, Y.J., Acton, T.B., and Montelione, G.T. (2014). DisMeta: a meta server for construct design and optimization. Methods Mol. Biol. 1091, 3–16.
34. Uversky, V.N., Radivojac, P., Iakoucheva, L.M., Obradovic, Z., and Dunker, A.K. (2007). Prediction of intrinsic disorder and its use in functional proteomics. Methods Mol. Biol. 408, 69–92.

35. Lupas, A., Van Dyke, M., and Stock, J. (1991). Predicting coiled coils from protein sequences. Science *252*, 1162–1164.

36. Holehouse, A.S., Das, R.K., Ahad, J.N., Richardson, M.O.G., and Pappu, R.V. (2017). CIDER: Resources to Analyze Sequence-Ensemble Relationships of Intrinsically Disordered Proteins. Biophys. J. *112*, 16–21.

37. Kyte, J., and Doolittle, R.F. (1982). A simple method for displaying the hydropathic character of a protein. J. Mol. Biol. *157*, 105–132.

38. Zarin, T., Strome, B., Nguyen Ba, A.N., Alberti, S., Forman-Kay, J.D., and Moses, A.M. (2019). Proteome-wide signatures of function in highly diverged intrinsically disordered regions. Elife *8*, e46883.

39. Kaewsuya, P., Danielson, N.D., and Ekhterae, D. (2007). Fluorescent determination of cardiolipin using 10-N-nonyl acridine orange. Anal. Bioanal. Chem. *387*, 2775–2782.

40. Planas-Iglesias, J., Dwarakanath, H., Mohammadyani, D., Yanamala, N., Kagan, V.E., and Klein-Seetharaman, J. (2015). Cardiolipin Interactions with Proteins. Biophys. J. *109*, 1282–1294.

41. Sathappa, M., and Alder, N.N. (2016). The ionization properties of cardiolipin and its variants in model bilayers. Biochim. Biophys. Acta *1858*, 1362–1372.

42. Belazi, D., Solé-Domènech, S., Johansson, B., Schalling, M., and Sjövall, P. (2009). Chemical analysis of osmium tetroxide staining in adipose tissue using imaging ToF-SIMS. Histochem. Cell Biol. *132*, 105–115.

43. Munnik, T., and Wierzchowiecka, M. (2013). Lipid-binding analysis using a fat blot assay. Methods Mol. Biol. *1009*, 253–259.

44. Potting, C., Tatsuta, T., König, T., Haag, M., Wai, T., Aaltonen, M.J., and Langer, T. (2013). TRIAP1/PRELI complexes prevent apoptosis by mediating intramitochondrial transport of phosphatidic acid. Cell Metabol. *18*, 287–295.

45. Ye, C., Shen, Z., and Greenberg, M.L. (2016). Cardiolipin remodeling: a regulatory hub for modulating cardiolipin metabolism and function. J. Bioenerg. Biomembr. *48*, 113–123.

46. Bota, D.A., and Davies, K.J.A. (2002). Lon protease preferentially degrades oxidized mitochondrial aconitase by an ATP-stimulated mechanism. Nat. Cell Biol. *4*, 674–680.

47. Choi, S.Y., Huang, P., Jenkins, G.M., Chan, D.C., Schiller, J., and Frohman, M.A. (2006). A common lipid links Mfn-mediated mitochondrial fusion and SNARE-regulated exocytosis. Nat. Cell Biol. *8*, 1255–1262.

48. Hatos, A., Tosatto, S., Vendruscolo, M., and Fuxreiter, M. (2022). FuzDrop on AlphaFold: visualizing the sequence-dependent propensity of liquid-liquid phase separation and aggregation of proteins. Nucleic Acids Res. *50*, W337–W344.

49. Banani, S.F., Rice, A.M., Peeples, W.B., Lin, Y., Jain, S., Parker, R., and Rosen, M.K. (2016). Compositional Control of Phase-Separated Cellular Bodies. Cell *166*, 651–663.

50. Lee, J.H., Park, A., Oh, K.J., Lee, S.C., Kim, W.K., and Bae, K.H. (2019). The role of adipose tissue mitochondria: Regulation of mitochondrial function for the treatment of metabolic diseases. Int. J. Mol. Sci. *20*, 4924.

51. Sidossis, L., and Kajimura, S. (2015). Brown and beige fat in humans: thermogenic adipocytes that control energy and glucose homeostasis. J. Clin. Invest. *125*, 478–486.

52. Fenzl, A., and Kiefer, F.W. (2014). Brown adipose tissue and thermogenesis. Horm. Mol. Biol. Clin. Invest. *19*, 25–37.

53. Crichton, P.G., Lee, Y., and Kunji, E.R.S. (2017). The molecular features of uncoupling protein 1 support a conventional mitochondrial carrier-like mechanism. Biochimie *134*, 35–50.

54. Castellana, M., Wilson, M.Z., Xu, Y., Joshi, P., Cristea, I.M., Rabinowitz, J.D., Gitai, Z., and Wingreen, N.S. (2014). Enzyme clustering accelerates processing of intermediates through metabolic channeling. Nat. Biotechnol. *32*, 1011–1018.

55. Prouteau, M., and Loewith, R. (2018). Regulation of Cellular Metabolism through Phase Separation of Enzymes. Biomolecules *8*, 160.

56. Strulson, C.A., Molden, R.C., Keating, C.D., and Bevilacqua, P.C. (2012). RNA catalysis through compartmentalization. Nat. Chem. *4*, 941–946.

57. Bracha, D., Walls, M.T., and Brangwynne, C.P. (2019). Probing and engineering liquid-phase organelles. Nat. Biotechnol. *37*, 1435–1445.

58. Zhao, E.M., Suek, N., Wilson, M.Z., Dine, E., Pannucci, N.L., Gitai, Z., Avalos, J.L., and Toettcher, J.E. (2019). Light-based control of metabolic flux through assembly of synthetic organelles. Nat. Chem. Biol. *15*, 589–597.

59. Hinzpeter, F., Gerland, U., and Tostevin, F. (2017). Optimal Compartmentalization Strategies for Metabolic Microcompartments. Biophys. J. *112*, 767–779.

60. Su, X., Ditlev, J.A., Hui, E., Xing, W., Banjade, S., Okrut, J., King, D.S., Taunton, J., Rosen, M.K., and Vale, R.D. (2016). Phase separation of signaling molecules promotes T cell receptor signaltransduction. Science *352*, 595–599.

61. Arakawa, H. (2023). MLOs and control of metabolic pathways. In Uversky V. Droplets of life, *Chapter14* (Elsevier), pp. 431–446.

62. Kim, T.H., Tsang, B., Vernon, R.M., Sonenberg, N., Kay, L.E., and Forman-Kay, J.D. (2019). Phospho-dependent phase separation of FMRP and CAPRIN1 recapitulates regulation of translation and deadenylation. Science *365*, 825–829.

63. Kojima, T., and Takayama, S. (2018). Membraneless Compartmentalization Facilitates Enzymatic Cascade Reactions and Reduces Substrate Inhibition. ACS Appl. Mater. Interfaces *10*, 32782–32791.

64. Feric, M., Vaidya, N., Harmon, T.S., Mitrea, D.M., Zhu, L., Richardson, T.M., Kriwacki, R.W., Pappu, R.V., and Brangwynne, C.P. (2016). Coexisting liquid phases underlie nucleolar subcompartments. Cell *165*, 1686–1697.

65. Peeples, W., and Rosen, M.K. (2021). Mechanistic dissection of increased enzymatic rate in a phase-separated compartment. Nat. Chem. Biol. *17*, 693–702.

66. Tatsuta, T., and Langer, T. (2008). Quality control of mitochondria: protection against neurodegeneration and aging. EMBO J. *27*, 306–314.

67. Hamada, K., Kurashige, T., Shimamura, M., Arakawa, H., Nakamura, Y., and Nagayama, Y. (2022). Mieap and ATG5 are tumor suppressors in a mouse model of BRAF^{V600E}-positive thyroid cancer. Front. Endocrinol. *13*, 932754.

68. Serricchio, M., Vissa, A., Kim, P.K., Yip, C.M., and McQuibban, G.A. (2018). Cardiolipin synthesizing enzymes form a complex that interacts with cardiolipin-dependent membrane organizing proteins. Biochim. Biophys. Acta Mol. Cell Biol. Lipids *1863*, 447–457.

69. Barnard, T., and Afzelius, B.A. (1972). The matrix granules of mitochondria: A review. Subcell. Biochem. *1*, 375–389.

70. Jacob, W.A., Bakker, A., Hertsens, R.C., and Biermans, W. (1994). Mitochondrial matrix granules: their behavior during changing metabolic situations and their relationship to contact sites between inner and outer mitochondrial membranes. Microsc. Res. Tech. *27*, 307–318.

71. Wilkins, M.R., Gasteiger, E., Bairoch, A., Sanchez, J.C., Williams, K.L., Appel, R.D., and Hochstrasser, D.F. (1999). Protein identification and analysis tools in the ExPASy server. Methods Mol. Biol. *112*, 531–552.

72. Schneider, C.A., Rasband, W.S., and Eliceiri, K.W. (2012). NIH Image to ImageJ: 25 years of image analysis. Nat. Methods *9*, 671–675.

73. Tsukada, T., Tomooka, Y., Takai, S., Ueda, Y., Nishikawa, S., Yagi, T., Tokunaga, T., Takeda, N., Suda, Y., Abe, S., et al. (1993). Enhanced proliferative potential in culture of cells from p53-deficient mice. Oncogene *8*, 3313–3322.

74. Nakamura, Y., Kitamura, N., Shinogi, D., Yoshida, M., Goda, O., Murai, R., Kamino, H., and Arakawa, H. (2012). BNIP3 and NIX mediate Mieap-induced accumulation of lysosomal proteins within mitochondria. PLoS One *7*, e30767.

75. Oda, K., Arakawa, H., Tanaka, T., Matsuda, K., Tanikawa, C., Mori, T., Nishimori, H., Tamai, K., Tokino, T., Nakamura, Y., and Taya, Y. (2000). p53AIP1, a potential mediator of p53-dependent apoptosis, and its regulation by Ser-46-phosphorylated p53. Cell *102*, 849–862.

76. Shindou, H., Koso, H., Sasaki, J., Nakanishi, H., Sagara, H., Nakagawa, K.M., Takahashi, Y., Hishikawa, D., Iizuka-Hishikawa, Y., Tokumasu, F., et al. (2017). Docosahexaenoic acid preserves visual function by maintaining correct disc morphology in retinal photoreceptor cells. J. Biol. Chem. *292*, 12054–12064.

77. Yamamoto, T., Endo, J., Kataoka, M., Matsuhashi, T., Katsumata, Y., Shirakawa, K., Yoshida, N., Isobe, S., Moriyama, H., Goto, S., et al. (2018). Decrease in membrane phospholipids unsaturation correlates with myocardial diastolic dysfunction. PLoS One *13*, e0208396.

78. Bligh, E.G., and Dyer, W.J. (1959). A rapid method of total lipid extraction and purification. Can. J. Biochem. *37*, 911–917.

STAR★METHODS

KEY RESOURCES TABLE

REAGENT or RESOURCE	SOURCE	IDENTIFIER
Antibodies		
Rabbit polyclonal anti-Mieap	Miyamoto et al.,[25] 2011	N/A
Mouse monoclonal anti-GFP	Santa Cruz	Cat# sc-9996; RRID: AB_627695
Mouse monoclonal anti-FLAG	Sigma Aldrich	Cat# F1804; RRID: AB_262044
Goat anti-rabbit IgG secondary antibody, Alexa Fluor 546	Thermo Fisher Scientific	Cat# A-11010; RRID: AB_2534077
Goat anti-mouse IgG secondary antibody, Alexa Fluor 546	Thermo Fisher Scientific	Cat# A-11003; RRID: AB_141370
Goat anti rabbit IgG 10 nm gold antibody	BBI Solutions	Cat# EM.GAR10; RRPD: AB_2715527
Rabbit polyclonal anti-GST	Santa Cruz	Cat# sc-459; RRID: AB_631586
Goat anti-rabbit IgG-HRP antibody	Santa Cruz	Cat# sc-2004; RRID: AB_631746
Bacterial and virus strains		
Ad-Mieap	Miyamoto et al.,[25] 2011	N/A
Ad-EGFP-Mieap	This paper	N/A
Ad-N-FLAG-Mieap	This paper	N/A
Ad-C-FLAG-Mieap	This paper	N/A
Ad-EGFP-MieapΔCC	This paper	N/A
Ad-EGFP-MieapΔ275	This paper	N/A
Ad-EGFP-MieapΔ496	This paper	N/A
Ad-Tag-RFP-T-Mieap	This paper	N/A
Ad-mApple-TOMM20	This paper	N/A
Ad-EGFP-BNIP3	This paper	N/A
Ad-EGFP-NIX	This paper	N/A
Ad-AcGFP1-Mito	This paper	N/A
Ad-DsRed2-Mito	This paper	N/A
Ad-EGFP-cytochrome *c*	This paper	N/A
Chemicals, peptides, and recombinant proteins		
T4 DNA polymerase	Thermo Fisher Scientific	Cat# 18005025
FuGENE 6	Promega	Cat# E2692
Triton X-100	Sigma Aldrich	Cat# 9002-93-1
Tween 20	Sigma Aldrich	Cat# P1379
VECTASHIELD Mounting Medium	Vector Laboratories	Cat# H-1000
MitoTracker Red CMXRos	Thermo Fisher Scientific	Cat# M7512
MitoTracker Green FM	Thermo Fisher Scientific	Cat# M7514
SYBR Green I	Thermo Fisher Scientific	Cat# S7563
Nonyl Acridine Orange	Thermo Fisher Scientific	Cat# A1372
Glutathione Sepharose 4B	Cytiva	Cat# 17075601
Cardiolipin, Bovine Heart, Sodium Salt	Olbracht Serdary Research Laboratories	Cat# A-42
L-α-Phosphatidylcholine, Bovine Heart	Olbracht Serdary Research Laboratories	Cat# A-301

Continued

REAGENT or RESOURCE	SOURCE	IDENTIFIER
L-α-Phosphatidylethanolamine, Bovine Heart	Olbracht Serdary Research Laboratories	Cat# A-341
Bovine Serum Albumin, Fatty Acid Free	FUJIFILM Wako Pure Chemical Corporation	Cat# 013-15143
Amersham Hybond P PVDF 0.45	Cytiva	Cat# 10600023
Amersham Hybond ECL Nitrocellulose Membrane	Cytiva	Cat# RPN68D
ECL Western Blotting Detection Reagents	Cytiva	Cat# 2106
XF DMEM medium pH 7.4	Agilent	Cat# 103575-100
XF 1.0 M Glucose Solution	Agilent	Cat# 103577-100
XF 200 mM Glutamine Solution	Agilent	Cat# 103579-100
2′,7′-Dichlorofluorescin diacetate	Sigma Aldrich	Cat# D6883
Critical commercial assays		
Zero Blunt TOPO PCR Cloning Kit	Thermo Fisher Scientific	Cat# 450245
QuikChange Site-Directed Mutagenesis Kit	Agilent	Cat# 200518
Agilent Seahorse XF Real-Time ATP Rate Assay Kit	Agilent	Cat# 103592-100
Deposited data		
The datasets generated during the mass spectrometric analyses of cardiolipin	This paper	Metabolomics Workbench repository, [https://www.metabolomicsworkbench.org/data/DRCCMetadata.php?Mode=Project&ProjectID=PR001192], under Project ID PR001192.
Experimental models: Cell lines		
A549	ATCC	Cat# CRM-CCL-185, RRID:CVCL_0023
U373MG	ATCC	Cat # HTB-17 RRID:CVCL_2219
LS174T	ATCC	Cat# CCL-188, RRID:CVCL_1384
293	ATCC	Cat# CRL-1573, RRID:CVCL_0045
HeLa	ATCC	Cat# CCL-2, RRID:CVCL_0030
HCT116	ATCC	Cat# CCL_247, RRID:CVCL_0291
Experimental models: Organisms/strains		
Mouse: C57BL/6J	CLEA Japan	N/A
Mouse: C57BL/6J Mieap deficient	Tsuneki et al.,[28] 2015	N/A
Oligonucleotides		
See Table S1	This paper	N/A
Recombinant DNA		
Plasmid: pEGFP-C1	Clontech	Cat# 632317
Plasmid: pEGFP-N1	Clontech	Cat# 632318
Plasmid: pCMV-Tag2	Agilent	Cat# 211172
Plasmid: p3xFLAG-CMV-14	Sigma Aldrich	Cat# E7908
Plasmid: pGEX5X-2	Cytiva	Cat# 27-4585-01
Plasmid: pcDNA3.1 (+)	Thermo Fisher Scientific	Cat# V79020
Plasmid: pEGFP-Mieap	This paper	N/A
Plasmid: pN-FLAG-Mieap	This paper	N/A
Plasmid: pC-FLAG-Mieap	This paper	N/A
Plasmid: pEGFP-MieapΔCC	This paper	N/A
Plasmid: pEGFP-MieapΔ275	This paper	N/A

Continued

REAGENT or RESOURCE	SOURCE	IDENTIFIER
Plasmid: pEGFP-MieapΔ496	This paper	N/A
Plasmid: pTagRFP-T-Mieap	This paper	N/A
Plasmid: pTagRFP-T-MieapΔCC	This paper	N/A
Plasmid: pTagRFP-T-MieapΔ275	This paper	N/A
Plasmid: pTagRFP-T-MieapΔ496	This paper	N/A
Plasmid: pCMV-Tag2B-BNIP3	This paper	N/A
Plasmid: pEGFP-BNIP3	This paper	N/A
Plasmid: pCMV-Tag2B-NIX	This paper	N/A
Plasmid: pEGFP-NIX	This paper	N/A
Plasmid: pAcGFP1-Mito	Clontech	Cat# 632432
Plasmid: pDsRed2-Mito	Clontech	Cat# 632421
Plasmid: pGST-Mieap	This paper	N/A
Plasmid: pN-EGFP	This paper	N/A
Plasmid: pC-EGFP	This paper	N/A
Plasmid: pEGFP-TAMM41	This paper	N/A
Plasmid: pEGFP-PGS1	This paper	N/A
Plasmid: pEGFP-PTPMT1	This paper	N/A
Plasmid: pEGFP-CRLS1	This paper	N/A
Plasmid: pEGFP-PLA2G6	This paper	N/A
Plasmid: pEGFP-TAZ	This paper	N/A
Plasmid: pEGFP-PRELI	This paper	N/A
Plasmid: pEGFP-LONP1	This paper	N/A
Plasmid: pEGFP-PLD6	This paper	N/A
Software and algorithms		
Metamorph ver. 7.8	Molecular Devices	https://www.moleculardevices.com/
cellSens Dimension	Olympus	https://www.olympus-lifescience.com/ja/software/cellsens/
OrthoDB v10	Kriventseva et al., 2019[32]	https://www.orthodb.org
Genetyx ver. 10	Genetyx Corporation	www.genetyx.co.jp/
VL3-BA	Uversky et al., 2007[34]	http://www.pondr.com/
DisMeta	Huang et al., 2014[33]	http://www-nmr.cabm.rutgers.edu/bioinformatics/disorder/
COILS	Lupas et al., 1991[35]	https://embnet.vital-it.ch/software/COILS_form.html
ProtScale	Wilkins et al., 1999[71]	https://web.expasy.org/protscale/
CIDER	Holehouse et al., 2017[36]	http://pappulab.wustl.edu/CIDER/
LipidSearch4.2 software	Mitsui knowledge industry	https://www.mki.co.jp/
Photoshop CC	Adobe	https://www.adobe.com/products/photoshop.html#
ImageJ	Schneider et al., 2012[72]	https://imagej.nih.gov/ij/
JMP 14.2.0	SAS	https://www.jmp.com
FuzDrop	Hatos et al., 2022[48]	https://fuzdrop.bio.unipd.it

RESOURCE AVAILABILITY

Lead contact

Further information and requests for reagent and resource may be directed to and will be fulfilled by the lead contact, Hirofumi Arakawa (harakawa@ncc.go.jp).

Materials availability

Plasmids generated in this study are available from the lead contact upon request.

Data and code availability

- All the data generated during the mass spectrometric analyses of cardiolipin in this study have been deposited at the Metabolomics Workbench repository (https://www.metabolomicsworkbench.org) and are publicly available as of the date of publication. Accession number is shown in the key resources table.
- This paper does not report original code.
- Any additional information required to reanalyze the data reported in this paper is available from the lead contact upon request.

EXPERIMENTAL MODEL AND STUDY PARTICIPANT DETAILS

Cell lines

The following cell lines were purchased from the American Type Culture Collection: A549 (tissue, lung cancer; gender, male), U373MG (tissue, glioblastoma; gender, male), LS174T (tissue, colon cancer; gender, female), HeLa (tissue, cervical cancer; gender, female), HCT116 (tissue, colon cancer; gender, male), and 293 (tissue, embryonic kidney). A549 cells were cultured in RPMI 1640 (Sigma). U373MG, LS174T, HeLa, and 293 cells were cultured in DMEM (Sigma). HCT116 cells were cultured in McCoy's 5A (Gibco). All media were supplemented with 10% fetal bovine serum. Cells were maintained at 37°C in a humidified chamber with 5% CO_2. These cell lines have not been authenticated.

We established a Mieap-KD cell line using LS174T, as previously described.[29] Mieap expression was inhibited in this cell line by retroviral expression of short hairpin RNA (shRNA) against the Mieap sequence. We also established LS174T-cont cells using a retroviral vector with a target sequence for EGFP, or an empty retroviral vector, and A549-cont cells using an empty retroviral vector.

Animals

Animal experiment protocols were approved by the Committee for Ethics in Animal Experimentation (approved protocol No. T17-043), and experiments were conducted in accordance with Guidelines for Animal Experiments of the National Cancer Center. All the animals used were in C57BL/6J background. C57BL/6J WT mice were obtained from CLEA Japan (Tokyo, Japan). Mieap-knockout (Mieap$^{-/-}$) mice were generated using the Cre/*loxP* recombination system, as previously reported.[32] Briefly, floxed and trapped alleles were generated using a single construct bearing a gene-trap cassette doubly flanked by *LoxP* and FRT, located between exons 5 and 8 of the mouse Mieap gene, which is located on chromosome 5. Mieap homozygous (Mieap$^{-/-}$) deficient mice were generated by mating breeding pairs of Mieap heterozygous (Mieap$^{+/-}$) mice. p53-deficient mice were a gift from Dr. S. Aizawa, Center for Developmental Biology, RIKEN.[73]

Female and male mice from 7 to 130 weeks old were housed at 22 ± 2°C with a 12 h light/dark cycle with free access to food, CE-2 (CLEA Japan), and water.

METHOD DETAILS

Plasmid construction

Constructs containing Mieap

For construction of the plasmid containing N-terminal EGFP-tagged Mieap, the nucleotide sequence of Mieap was PCR-amplified using primers N-EGFP-Mieap-F and N-EGFP-Mieap-R. PCR products were digested with Kpn I and ligated into pEGFP-C1 (Clontech) cut with the same enzyme. For construction of the plasmid containing C-terminal EGFP-tagged Mieap, the nucleotide sequence of Mieap, excluding the stop codon, was PCR-amplified using the primers C-EGFP-Mieap-F and C-EGFP-Mieap-R. PCR products were ligated into the pCR-Blunt II-TOPO vector (Thermo Fisher Scientific) and sequenced. Inserted products were excised using Hind III restriction sites, and ligated into pEGFP-N1 (Clontech), cut with the same enzyme. N-terminal EGFP-tagged Mieap was used as EGFP-Mieap, except for Figures 1A–1D and Video S3 where the C-terminal EGFP-tagged Mieap was used.

Plasmids containing N-FLAG-Mieap (pN-FLAG-Mieap) were constructed as follows. The nucleotide sequence of Mieap was PCR-amplified using the primers, N-FLAG-Mieap-F and N-FLAG-Mieap-R. PCR products were ligated into the pCR-Blunt II-TOPO vector (Thermo Fisher Scientific) and sequenced. Inserted products were excised using the Kpn I restriction sites and ligated into pre-digested pcDNA3.1 (+) (Thermo Fisher Scientific) cut with the same enzyme. The nucleotide sequence of Mieap was excised from the plasmid using the Hind III and Xho I restriction sites, and ligated into pre-digested pCMV-Tag2A (Agilent) cut with the same enzyme.

The plasmid containing C-FLAG-Mieap (pC-FLAG-Mieap) was constructed as follows. The nucleotide sequence of Mieap, excluding the stop codon, was PCR-amplified using the primers, C-EGFP-Mieap-F and C-EGFP-Mieap-R, the same primers used for construction of the plasmid containing C-terminal EGFP-tagged Mieap. PCR products were ligated into the pCR-Blunt II-TOPO vector (Thermo Fisher Scientific) and sequenced. Inserted products were excised using the Hind III restriction site and ligated into pre-digested p3xFLAG-CMV-14 (Sigma Aldrich) cut with the same enzyme.

Prior to construction of plasmids containing EGFP-Mieap deletion mutants, point mutations in Bgl II, Sac I, EcoR I, and Pst I restriction sites of the multiple cloning site of pEGFP-Mieap were introduced using QuikChange Site-Directed Mutagenesis Kits (Agilent) with primers Mut-F1, Mut-R1, Mut-F2 and Mut-R2, which were confirmed by DNA sequencing.

For construction of plasmids containing EGFP-MieapΔCC (pEGFP-MieapΔCC), the nucleotide sequence of pEGFP-Mieap between two Pst I restriction sites was deleted by digestion with Pst I. The remainder was self-ligated, additionally deleting c.810C using the QuikChange Site-Directed Mutagenesis Kit (Agilent) with primers Mut-F3 and Mut-R3 to make the deletion mutation in-frame.

For construction of plasmids containing EGFP-MieapΔ275 (pEGFP-MieapΔ275), the nucleotide sequence of pEGFP-Mieap between the Bgl II and Sma I restriction sites was deleted by digestion using Bgl II and Sma I. After blunting with T4 DNA polymerase (Thermo Fisher Scientific), the remainder was self-ligated.

For construction of plasmids containing EGFP-MieapΔ496 (pEGFP-MieapΔ496), the nucleotide sequence of pEGFP-Mieap was deleted between the EcoR I and Kpn I restriction sites by digestion using EcoR I and Kpn I. After blunting with T4 DNA polymerase (Thermo Fisher Scientific), the remainder was self-ligated.

For construction of plasmids containing TagRFP-T-Mieap (pTagRFP-T-Mieap), the nucleotide sequence of pEGFP-Mieap between the Nhe I and Xho I restriction sites containing EGFP was replaced with nucleotide sequence of pTagRFP-T-EEA1 (Addgene #42635) between the Nhe I and Xho I restriction sites containing TagRFP-T, by digestion using Nhe I and Xho I.

For construction of plasmids containing GST-Mieap (pGST-Mieap), the nucleotide sequence of Mieap (amino acids 99–298) was PCR-amplified using the primers, GST-Mieap-F and GST-Mieap-R. PCR products were ligated into the pCR-Blunt II-TOPO vector (Thermo Fisher Scientific) and sequenced. Products were digested with EcoR I and Xho I, and ligated into pGEX5X-2 (Cytiva).

For construction of plasmids containing Mieap ΔCC (pMieap ΔCC), pEGFP-Mieap ΔCC was digested at the Kpn I restriction sites to obtain the nucleotide sequence of Mieap ΔCC, and ligated into pcDNA3.1 (+) (Thermo Fisher Scientific) cut with the same enzyme, Kpn I.

For construction of plasmids containing Mieap Δ274 (pMieap Δ274), the nucleotide sequence of Mieap Δ274 was PCR-amplified from pEGFP- Mieap Δ275 using the primers, Δ274-F and Δ274-R. PCR products were digested with Kpn I, and ligated into pcDNA3.1 (+) (Thermo Fisher Scientific) cut with the same enzyme, Kpn I.

For construction of plasmids containing Mieap Δ496 (pMieap Δ496), pEGFP-Mieap Δ496 was subjected to inverse PCR using the primers, ΔEGFP-F and ΔEGFP-R to delete the nucleotide sequence of EGFP from pEGFP-Mieap Δ496, and the product was self-ligated using KOD-Plus-Mutagenesis Kit (TOYOBO).

Prior to construction of plasmids containing TagRFP-T-Mieap deletion mutants, the nucleotide sequence of TagRFP-T was PCR-amplified using the primers, TagRFP-T-F and TagRFP-T-R. PCR products were digested with Hind III and EcoR V, and ligated into pcDNA3.1 (+) (Thermo Fisher Scientific) cut with the same enzymes (pcDNA-N-TagRFP). The nucleotide sequence of Mieap was PCR-amplified using the primers, G35-F and G35-R. PCR products were digested with EcoRV and PspOMI, and ligated into pcDNA-N-TagRFP cut with the same enzymes (pG35).

For construction of plasmids containing TagRFP-T-Mieap ΔCC (pTagRFP-T-Mieap ΔCC), pG35 was subjected to inverse PCR using the primers, ΔCC-F and ΔCC-R, and the product was self-ligated using KOD-Plus-Mutagenesis Kit (TOYOBO).

For construction of plasmids containing TagRFP-T-Mieap Δ275 (pTagRFP-T-Mieap ΔCC), pTagRFP-T-Mieap was subjected to inverse PCR using the primers, Δ275-F and Δ275-R, and the product was self-ligated using KOD-Plus-Mutagenesis Kit (TOYOBO).

For construction of plasmids containing TagRFP-T-Mieap Δ496 (pTagRFP-T-Mieap Δ496), pG35 was subjected to inverse PCR using the primers, Δ496-F and Δ496-R, and the product was self-ligated using KOD-Plus-Mutagenesis Kit (TOYOBO).

All primers are listed in Table S1.

Other constructs

For construction of plasmids containing EGFP-BNIP3 (pEGFP-BNIP3), plasmids containing FLAG-BNIP3 (pCMV-Tag2B-BNIP3) were constructed in advance. For construction of the pCMV-Tag2B-BNIP3, the nucleotide sequence of BNIP3 was PCR-amplified using the primers, BNIP3-F and BNIP3-R. PCR products were ligated into the pCR-Blunt II-TOPO vector (Thermo Fisher Scientific) and sequenced. Inserted products were digested with EcoR I and Xho I, and ligated into the pre-digested pCMV-Tag2B (Agilent) cut with the same enzyme. The nucleotide sequence of pCMV-Tag2B-BNIP3 was digested at the EcoR I and Xho I restriction sites, and subsequently blunted with T4 DNA polymerase (Thermo Fisher Scientific). pEGFP-C1 (Clontech) was digested with Bgl II, blunted with T4 DNA polymerase, self-ligated, digested with EcoR I and Sma I, and ligated with the fragment of pCMV-Tag2B-BNIP3.

For construction of plasmids containing EGFP-NIX (pEGFP-NIX), plasmids containing FLAG-NIX (pCMV-Tag2B-NIX) were constructed in advance. For construction of the pCMV-Tag2B-NIX, the nucleotide sequence of NIX was PCR-amplified using the primers, NIX-F and NIX-R. PCR products were ligated into the pCR-Blunt II-TOPO vector (Thermo Fisher Scientific) and sequenced. Inserted products were digested with EcoR I and Xho I, and ligated into pre-digested pCMV-Tag2B (Agilent) cut with the same enzyme. The nucleotide sequence of pCMV-Tag2B-NIX was digested at the EcoR I and Xho I restriction sites, and subsequently blunted with T4 DNA polymerase (Thermo Fisher Scientific). pEGFP-C1 (Clontech) was digested with Bgl II, blunted with T4 DNA polymerase, self-ligated, digested with EcoR I and Sma I, and ligated with the fragment of pCMV-Tag2B-NIX.

For construction of the plasmid backbone containing EGFP (pN-EGFP), the nucleotide sequence of EGFP, excluding the stop codon, was PCR-amplified using the primers, N-EGFP-F and N-EGFP-R. PCR products were digested with Hind III and BamH I, and ligated into pcDNA3.1 (+) (Thermo Fisher Scientific) cut with the same enzymes.

For construction of the plasmid backbone containing EGFP (pC-EGFP), the nucleotide sequence of EGFP was PCR-amplified using the primers, C-EGFP-F and C-EGFP-R. PCR products were digested with BamH I and Not I, and ligated into pcDNA3.1 (+) (Thermo Fisher Scientific) cut with the same enzymes.

For construction of plasmids containing EGFP-TAMM41 (pEGFP-TAMM41), the nucleotide sequence of TAMM41, excluding the stop codon, was PCR-amplified using the primers, TAMM41-F and TAMM41-R. PCR products were digested with Nhe I and BamH I, and ligated into pC-EGFP cut with the same enzymes.

For construction of plasmids containing EGFP-PGS1 (pEGFP-PGS1), the nucleotide sequence of PGS1, excluding stop codon, was PCR-amplified using the primers, PGS1-F and PGS1-R. PCR products were digested with Hind III and BamH I and ligated into pC-EGFP cut with the same enzymes.

For construction of plasmids containing EGFP-PTPMT1 (pEGFP-PTPMT1), the nucleotide sequence of PTPMT1, excluding the stop codon, was PCR-amplified using the primers, PTPMT1-F and PTPMT1-R. PCR products were digested with Nhe I and Hind III and ligated into pC-EGFP cut with the same enzymes.

For construction of plasmids containing EGFP-CRLS1 (pEGFP-CRLS1), the nucleotide sequence of CRLS1 was PCR-amplified using the primers, CRLS1-F and CRLS1-R. PCR products were digested with BamH I and Not I and ligated into pN-EGFP cut with the same enzymes.

For construction of plasmids containing EGFP-PLA2G6 (pEGFP-PLA2G6), the nucleotide sequence of PLA2G6, excluding the stop codon, was PCR-amplified using the primers, PLA2G6-F and PLA2G6-R. PCR products were digested with Nhe I and Kpn I and ligated into pC-EGFP cut with the same enzymes.

For construction of plasmids containing EGFP-TAZ (pEGFP-TAZ), the nucleotide sequence of TAZ, excluding the stop codon, was PCR-amplified using the primers, TAZ-F and TAZ-R. PCR products were digested with Nhe I and Kpn I and ligated into pC-EGFP cut with the same enzymes.

For construction of plasmids containing EGFP-PRELI (pEGFP-PRELI), the nucleotide sequence of PRELI, excluding the stop codon, was PCR-amplified using the primers, PRELI-F and PRELI-R. PCR products were digested with Nhe I and BamH I and ligated into pC-EGFP cut with the same enzymes.

For construction of plasmids containing EGFP-LONP1 (pEGFP-LONP1), the nucleotide sequence of LONP1, excluding the stop codon, was PCR-amplified using the primers, LONP1-F and LONP1-R. PCR products were digested with Hind III and BamH I and ligated into pC-EGFP cut with the same enzymes.

For construction of plasmids containing EGFP-PLD6 (pEGFP-PLD6), the nucleotide sequence of PLD6, excluding the stop codon, was PCR-amplified using the primers, PLD6-F and PLD6-R. PCR products were digested with Nhe I and Kpn I and ligated into pC-EGFP cut with the same enzymes.

All primers are listed in Table S1.

Transfection

For transfection, cells were seeded (2×10^5 cells/dish) in 35-mm glass bottom dishes. Plasmids (2 µg/dish) were transfected using FuGENE6 transfection reagent (Promega), according to the manufacturer's instructions.

Recombinant adenovirus construction

Ad-Mieap was derived from viruses as previously reported.[29,35,74] Replication-deficient recombinant viruses Ad-EGFP-Mieap, Ad-N-FLAG-Mieap, Ad-C-FLAG-Mieap, Ad-EGFP-MieapΔCC (Δ104-270), Ad-EGFP-MieapΔ275, Ad-EGFP-MieapΔ496, Ad-TagRFP-T-Mieap, Ad-mApple-TOMM20 derived from mApple-TOMM20-N-10 (Addgene #54955), Ad-EGFP-BNIP3, Ad-EGFP-NIX, Ad-AcGFP1-Mito, and Ad-DsRed2-Mito were generated from the corresponding plasmid vectors and purified as described previously.[75] Briefly, DNA fragments obtained by restriction of each plasmid vector were blunted using T4 DNA polymerase, ligated into the SmiI site of the cosmid, pAxCAwtit (Takara), which contains the CAG promoter and the entire genome of type 5 adenovirus, except the E1 and E3 regions. Recombinant adenoviruses were generated by *in vitro* homologous recombination in the 293 cell line with the cDNA-inserted pAxCAwtit and the adenovirus DNA terminal–protein complex. Viruses were propagated in the 293 cell line and purified by two rounds of CsCl density centrifugation. Viral titers were determined with a limiting dilution bioassay using 293 cells.

Adenoviral infection

Infection of cell lines was carried out by adding viral solutions to cell monolayers, incubating them at 37°C for 120 min with brief agitation every 20 min. This was followed by addition of culture medium and return of the infected cells to the 37°C incubator.

Immunocytochemistry

For immunocytochemistry, cells were grown on 8-well chamber slides (1-4×10^4 cells/well) at 37°C in conventional culture medium, and fixed in paraformaldehyde (Figure S1A, 2%; Figure S1B, 4%) for 15 min at room temperature. Slides were incubated with Triton X-100 (Figure S1A, 0.1% for 2 min; Figure S1B, 0.5% for 10 min), and washed 3x with phosphate-buffered saline (PBS) at room temperature. Cells were blocked with 3% bovine serum albumin (BSA) in PBS (Figure S1A, for 3 h; Figure S1B, for 2 h), and sequentially incubated with rabbit polyclonal anti-Mieap antibody (1:200), mouse monoclonal anti-GFP antibody (1:200), or mouse monoclonal anti-FLAG antibody (1:1000) for 2 h at room temperature. After washing 3x with PBS, slides were incubated with Alexa Fluor 546 goat anti-rabbit IgG antibody (1:200) or Alexa Fluor 546 goat anti-mouse IgG antibody (1:200) at room temperature (Figure S1A, for 2 h; Figure S1B, for 1 h). Slides were washed 3x with PBS. Then they were

mounted with VECTASHIELD H-1000 (Vector Laboratories) and observed using an FLUOVIEW FV3000 confocal laser scanning microscope (Olympus).

Histological analysis

Hematoxylin and eosin (HE) staining was performed using Eosin (CS701, Dako) and Hematoxylin (S2020, Dako). Immunohistochemistry (IHC) was performed as described previously.[28] Briefly, for antigen retrieval, paraffin-fixed sections were autoclaved in citric acid buffer (pH 6.0) at 121°C for 10 min. Sections were treated with 0.3% hydrogen peroxide in methanol for 30 min at room temperature to block endogenous peroxidase activity and incubated with 5% bovine serum albumin (BSA) in 50 mM Tris-buffered saline (pH 7.4) containing 0.05% Triton X-100 (T-TBS) for 1 h at room temperature to block non-specific protein binding sites. Sections were then incubated at 4°C with the primary antibodies, rabbit polyclonal anti-mouse Mieap antibody (1:1000),[28] and mouse monoclonal anti-cytochrome c (ab13575, 1 μg/mL) in TBS-T. After overnight incubation, sections were incubated with EnVision + Dual Link System-HRP reagents (Dako) for 1 h according to the manufacturer's instructions at room temperature and treated with 0.02% DAB (DOJINDO) in 0.05 M Tris-HCl buffer (pH 7.6). Finally, sections were counterstained with Hematoxylin (Dako). For immunofluorescence (IF), rabbit polyclonal anti-mouse Mieap antibody (1:1000),[28] and mouse monoclonal anti-cytochrome c (ab13575, 1 μg/mL) were used for primary antibodies. Alexa Fluor 594 goat antirabbit IgG antibody (1:200) and Alexa Fluor 488 goat anti-mouse IgG antibody (1:100) were used for secondary antibodies. Nuclear staining was performed with Hoechst 33342 (10 μg/mL) or TO-PRO-3 (200 nM).

Transmission electron microscopy (TEM)

A549-cont and U373MG cells (4×10^4 cells/24-well plate) were infected with Ad-Mieap. On day 1 after infection, cells were fixed in phosphate buffered 2.5% glutaraldehyde and subsequently post-fixed in 1% OsO_4 at 4°C for 2 h. Then, specimens were dehydrated in a graded ethanol series and embedded in epoxy resin. Ultrathin sections (75 nm) were cut with an ultramicrotome. Ultrathin sections stained with uranyl acetate and lead staining solution were observed on a transmission electron microscope H-7500 (Hitachi) at 80 kV.

LS174T (control and Mieap-KD) cells cultured under normal conditions were also processed for TEM as mentioned above, with the following modifications. 2% glutaraldehyde was used for prefixation. 2% OsO_4 was used instead for post-fixation. 80-90-nm ultrathin sections were cut and observed on a transmission electron microscope H-7600 (Hitachi) at 100 kV.

Kidney and liver specimens were collected from an 18-week-old WT mouse and a 16-week-old Mieap$^{-/-}$ male mouse. BAT specimens were collected from a 40-week-old WT and a 40-week-old Mieap$^{-/-}$ male mouse. Specimens cut into approximately $3 \times 3 \times 3$ mm^3 were also processed for TEM and processed in the same fashion as the aforementioned A549-cont cells. However, a mixture of 2% paraformaldehyde and 2% glutaraldehyde was used for prefixation.

Post-embedding immunoelectron microscopy

A549-cont cells (2×10^5 cells/35-mm glass bottom dish) were infected with Ad-Mieap. On day 1 after infection, cells were fixed with 4% paraformaldehyde and 0.025% glutaraldehyde in 0.1 M PBS (pH 7.4) for 1 h at 4°C. After fixation, cells were washed with 0.1 M PBS (pH 7.4) for 16 h at 4°C, dehydrated in a graded ethanol series, and infiltrated with LR White resin. Polymerization was performed in TAAB embedding capsules (TAAB) inverted on glass-bottom dishes for 3 h at 60°C. Ultrathin sections (75 nm) were collected on nickel grids. After blocking with 3% BSA in PBS for 1 h, sections were incubated with anti-Mieap antibody (1:200) diluted in PBS with 0.05% Triton X-100 for 2 h at RT. Sections were washed 8x with 0.15% glycine in PBS, and incubated with goat anti-rabbit IgG 10-nm gold antibody (1:50) diluted in PBS with 0.05% Triton X-100 for 2 h at RT. Sections were washed 8x in PBS and fixed with 1% glutaraldehyde in PBS for 5 min. Sections were washed 8x in distilled water. Grids were embedded in a mixture containing 2.7% polyvinyl alcohol and 0.3% uranyl acetate. Sections on grids were observed on a transmission electron microscope H-7500 (Hitachi) at 75 kV.

Amino acid sequence analyses of Mieap protein

We analyzed the phylogenetic spread of Mieap orthologs using OrthoDB v10 (https://www.orthodb.org/).[37] Multiple sequence alignment for Mieap orthologs was performed using Genetyx ver. 10. Prediction of IDRs in the amino acid sequence of Mieap was done using VL3-BA[39] on the PONDR server (http://www.pondr.com/) and collated with meta-prediction of IDRs using DisMeta (http://www-nmr.cabm.rutgers.edu/bioinformatics/disorder/).[38] Prediction of coiled-coil regions was done using COILS (https://embnet.vital-it.ch/software/COILS_form.html).[40] Hydrophobicity of Mieap was analyzed according to the Kyte-Doolittle index[42] using ProtScale (https://web.expasy.org/protscale/).[71] The linear net charge per residue of Mieap was analyzed using CIDER (http://pappulab.wustl.edu/CIDER/).[41] We analyzed the sequence-dependent propensity of liquid-liquid phase separation on Mieap and CL metabolic enzymes using FuzDrop server (https://fuzdrop.bio.unipd.it).[48]

Analyses of confocal microscopy image data

Throughout the study, confocal microscopy images were taken with an FLUOVIEW FV3000 confocal laser scanning microscope (Olympus). For validation of the spatial relationship between Mi-BCs and mApple-TOMM20, additional images were taken using a SpinSR10 spinning disk confocal super resolution microscope (Olympus). For z stack and time-lapse imaging, a montage of differential interference contrast (DIC) and fluorescence images was created using MetaMorph ver. 7.8 (Molecular Devices). 3D reconstruction was performed using cellSens Imaging Software (Olympus). Line-scan profiles were acquired using MetaMorph ver. 7.8 (Molecular Devices).

FRAP experiments

EGFP-Mieap, EGFP-MieapΔCC, EGFP-MieapΔ275, and EGFP-MieapΔ496 were expressed in A549-cont cells to generate condensates by infection with Ad-EGFP-Mieap, Ad-EGFP-MieapΔCC, Ad-EGFP-MieapΔ275, and Ad-EGFP-MieapΔ496, respectively. FRAP experiments were performed on an FLUOVIEW FV3000 confocal laser scanning microscope (Olympus), using a 60x/1.4 NA oil immersion objective (Olympus). Condensates were subjected to spot-bleaching or full-bleaching (bleaching entire condensates). For spot-bleaching, the bleaching area was unified to a diameter of 1.38 μm. Condensates were imaged for 6 s, acquiring 30 images prior to spot-bleaching or 50 s, acquiring 5 images prior to full-bleaching. Photobleaching employed a 488-nm laser at 10% laser power with 11.6 μs/μm exposure time or 1.4% laser power with 1.4 μs/μm exposure time. Time-lapse images were acquired at 0.2-ms intervals for 60 s or 10 s intervals for 15 min. Spot-bleaching data for each construct were acquired from 15 different condensates. Full-bleaching data of each construct were acquired from 10 different condensates.

Calculation of intensity ratio

To evaluate partitioning of EGFP-Mieap and deletion mutant proteins, EGFP-Mieap WT, ΔCC, Δ275, and Δ496 were expressed in A549-cont cells to generate condensates by infection with Ad-EGFP-Mieap WT, ΔCC, Δ275, and Δ496, respectively. EGFP intensity of condensates and cytoplasm was measured. Because EGFP intensity of these condensates was higher than the intensity of 0.4 mg/mL His-EGFP solution for standard curve, we chose intensity ratio rather than partition coefficient for the parameter of this partitioning experiments.[49] Intensity ratio was calculated as (Intensity of condensates-Intensity of background)/(Intensity of cytoplasm-Intensity of background), where Intensity of condensates, Intensity of cytoplasm, and Intensity of background are the mean intensities of condensates, cytoplasm, and PBS acquired by the identical conditions (laser wavelength, 488 nm; laser transmissivity, 0.01%; detection wavelength, 500–600 nm; voltage, 350 V) on an FLUOVIEW FV3000 confocal laser scanning microscope (Olympus). Intensity ratio data were obtained from 40 cells for each construct.

Expression and purification of GST and GST-Mieap

Escherichia coli (BL21) cells transformed with expression vectors were grown in 200 mL of Luria-Bertani medium at 37°C until the OD600 was between 0.55 and 0.6. Protein expression was induced with 100 μM IPTG, and bacteria were subsequently incubated for 3 h at 25°C. After harvesting bacteria by centrifugation at 3000 × *g* for 10 min at 4°C, pellets were lysed with lysis buffer (1% Triton X-100 buffered in PBS supplemented with 1 mM Phenylmethylsulfonyl fluoride), and sonicated (20 × 30 s bursts with 10 s rest between bursts). Insoluble material was removed by centrifugation at 10,000 rpm for 30 min at 4°C. Supernatant was incubated with glutathione Sepharose 4B (Cytiva) pre-equilibrated with lysis buffer at 4°C overnight. After the beads were washed twice with lysis buffer, proteins were eluted with elution buffer (50 mM glutathione diluted in 50 mM Tris–HCl, pH 8.0), and dialyzed at 4°C overnight against PBS.

Lipid-binding analysis

For lipid-binding analysis, protein-lipid interactions on lipid-spotted membranes were evaluated with fat blot assays.[43] Natural CL, PC, and PE derived from bovine heart (Olbracht Serdary Research Laboratories) were diluted with chloroform/methanol/1N HCl (80:80:1). 1 μL of each diluted lipid was spotted onto PVDF membranes (Cytiva) for antigen-antibody reactions using anti-Mieap antibody or nitrocellulose membranes (Cytiva) for antigen-antibody reactions using an anti-GST antibody to align spots with increasing amounts of lipids ranging from 0 to 667 pmol. Here, approximate molarities of CL, PC, and PE calculated from molecular weights of tetralinoleoyl CL, distearoyl PC, and distearoyl PC were used, respectively. After membranes were blocked with blocking buffer (3% fatty acid-free BSA diluted in 50 mM Tris–HCl, 150 mM NaCl, pH 7.5) for 1 h, membranes were incubated with 2.5 μg/mL of GST-Mieap or GST protein diluted in blocking buffer containing 0.1% Tween 20 overnight. Membranes were incubated with primary antibody (rabbit anti-Mieap antibody or rabbit anti-GST antibody) diluted in blocking buffer containing 0.06% Tween 20 (1:1000) for 3.5 h, and subsequently a secondary antibody (goat anti-rabbit antibody conjugated to horseradish peroxidase) diluted in blocking buffer containing 0.06% Tween 20 (1:10000) for 1 h. ECL Western Blotting Detection Reagents (Cytiva) was used to detect HRP and chemiluminescence was visualized with an ImageQuant LAS 4000 system (Cytiva).

Lipid preparation

Lipid preparation was performed as described previously.[76,77] Briefly, total lipids were extracted from samples using the Bligh-Dyer method.[78] An aliquot of the organic phase was added to an equal volume of methanol before being loaded onto a DEAE-cellulose column (Wako Chemical) pre-equilibrated with chloroform. After successive washes with chloroform/methanol (1:1, v/v), acidic phospholipids were eluted with chloroform/methanol/HCl/water (12:12:1:1, v/v), followed by evaporation to dryness to yield a residue was soluble in methanol.

Mass spectrometric analyses of CL

Analyses were performed on an LC/MS/MS system consisting of a Q-Exactive Plus mass spectrometer (Thermo Fisher Scientific) equipped with an electrospray ionization source and an UltiMate 3000 system (Thermo Fisher Scientific). Lipid samples were separated on a Waters X-Bridge C_{18} column (3.5 μm, 150 mm × 1.0 mm i.d.) at 40°C using a solvent step-gradient as follows: mobile phase A (isopropanol/methanol/water (5:1:4, v/v/v) supplemented with 5 mM ammonium formate and 0.05% ammonium hydroxide (28% in water))/mobile phase B (isopropanol supplemented with 5 mM ammonium formate and 0.05% ammonium hydroxide (28% in water)) ratios of 60%/40% (0 min), 40%/60% (1 min), 20%/80% (9 min), 5%/95% (11–30 min), 95%/5% (31–35 min) and 60%/40% (45 min). Flow rate was 25 μL/min. Source and ion transfer

parameters applied were as follows. Spray voltage was 3.0 kV. For negative ionization modes, the sheath gas and capillary temperatures were maintained at 60 and 320°C, respectively. The Orbitrap mass analyzer was operated at a resolving power of 70,000 in full-scan mode (scan range: 200–1800 m/z; automatic gain control (AGC) target:3e6) and of 35,000 in the Top 20 data-dependent MS2 mode (stepped normalized collision energy: 20, 30 and 40; isolation window: 4.0 m/z; AGC target: 1e5). Identification of CL molecular species was performed using LipidSearch 4.2 software (Mitsui Knowledge Industry).

Real-time ATP rate assay

LS174T-cont and Mieap-KD cells were seeded at a density of 2.5×10^4 cells/well (n = 9) on a Seahorse XF24 Cell Culture Microplate. Cells were incubated at 37°C in a humidified chamber with 5% CO_2. 18 h after seeding, culture medium was replaced with XF DMEM medium pH 7.4 supplemented with 25 mM glucose and 2 mM L-glutamine through three washes.

HCT116 cells were seeded at a density of 0.8×10^6 cells/60-mm dish (n = 9). Cells were incubated at 37°C in a humidified chamber with 5% CO_2. 24 h after seeding, cells were treated with Ad-Mieap or Ad-empty. 24 h after infection, cells were reseeded at a density of 4×10^4 cells/ well (n = 9) on a SeahorseXF24 Cell Culture Microplate. 20 h after reseeding, culture medium was replaced with XF DMEM medium pH 7.4 supplemented with 25 mM glucose and 2 mM L-glutamine through three washes.

After cells were incubated at 37°C in a non-CO_2 incubator for 60 min, cell culture plates were loaded into a Seahorse XFe24 Analyzer. Oxygen consumption rate (OCR) and extracellular acidification rate (ECAR) were recorded before and after serial injections of oligomycin and rotenone/antimycin A to yield final concentrations of 0.5 μM.

Flow cytometric analysis

LS174T-cont and Mieap-KD cells cultured under normal conditions were harvested by trypsin-EDTA treatment. After adding complete growth media to inactivate trypsin, cells were centrifuged, washed with PBS, and incubated with 5 μM 2′,7′-dichlorofluorescin-diacetate (Sigma) for 20 min at 37°C. After being washed with PBS, cells were immediately analyzed with an EC800 flow cytometry analyzer (Sony) using the 488-nm line.

Primers

The information of all PCR primers is indicated in Table S1.

QUANTIFICATION AND STATISTICAL ANALYSIS

FRAP data quantification

Fluorescence recovery rates were calculated using cellSens Imaging Software (Olympus), in which the intensity initially acquired after bleaching was set to 0 and the pre-bleaching intensity was set to 1. The normalized average fluorescence recovery was plotted in JMP 14.2.0 (SAS).

Crista data quantification

For quantification of crista data, crista area and outlines of mitochondrial sections in TEM images were marked manually using Adobe Photoshop CC, where normal crista morphology was identified by the presence of lamellar structures with distinct OsO_4 staining. Aberrant crista-like structures that were not observed in mitochondria of WT were excluded. Subsequently, the ratio of crista area per mitochondrial section was calculated from the indicated number of mitochondria in legends of Figures 7D, 7L, 7M, and 8E, using ImageJ.[72]

Statistical analysis

Statistical analyses were performed in JMP 14.2.0 (SAS). Levels of significance in Figures 5I, 7A, 7B, 7D, 7H–7J, 7L, 7N, 8A–8C, 8E, S7, S10B–S10D, and S10F–S10H were assessed using Student's two-tailed t tests. Levels of significance in mass spectrometric analyses for biological replicate pairs shown in Figures 4A, 4B, 7E, and 7F were assessed using the paired two-tailed t-test. $p < 0.05$ was considered statistically significant. Asterisks were allotted to all the Figures containing statistical analyses as follows: *, $p < 0.05$; **, $p < 0.01$, ***, $p < 0.001$, ****, $p < 0.0001$.

Data visualization

Visualization of the experimental data subjected to statistical analyses were performed using Graph Builder engine in JMP 14.2.0 (SAS). When the data were visualized using violin plots, boxplots were overlaid. The center line in the box indicates the median. The bottom and top of the box indicate the 25th and 75th percentiles. The whiskers extend 1.5 times the interquartile range (IQR) from the top and bottom of the box unless the minimum and maximum values are within the IQR. The values which fall above or below the whiskers are plotted individually as outliers.